Elettore, E., Freddi, F., Latour, M., Rizzano, G. (2022). Parametric study and finite element analysis of self-centring steel column bases with different structural properties, 199, 107628, https://doi.org/10.1016/j.jcsr.2022.107628

PARAMETRIC STUDY AND FINITE ELEMENT ANALYSIS OF SELF-CENTRING STEEL COLUMN BASES WITH DIFFERENT STRUCTURAL PROPERTIES

Elena Elettore[1*], Fabio Freddi[2], Massimo Latour[1], Gianvittorio Rizzano[1]

[1] *Department of Civil Engineering, University of Salerno, Italy*
[2] *Department of Civil, Environmental and Geomatic Engineering, University College London, UK*
[*] *Corresponding Author. Tel.: +39 3276933946; E-mail address: eelettore@unisa.it*

ABSTRACT

In recent years there have been significant advancements in the definitions of innovative seismic-resilient structural systems, chasing the urgent needs of reducing the repair costs and downtime in the aftermath of severe earthquake events. In this regard, self-centring Column Bases (CBs) represent a promising solution to improve the seismic performance of steel Moment Resisting Frames (MRFs) for both damage and residual drifts reductions. However, although several technologies have been conceived, studied, and experimentally tested in this direction, only a few research studies investigated the significant properties of the connections influencing the behaviour of these systems. Focusing on the steel damage-free Self-Centring Column Base (SC-CB) previously investigated by the authors, the present study performs a parametric Finite Element (FE) analysis to evaluate the influence of some design parameters over the global and local response of these joints, considering the objectives of obtaining a self-centring behaviour, as well as minimizing the yielding of the joint components. With this scope, an advanced FE model is developed in ABAQUS and validated against experimental results. FE models of three SC-CBs belonging to different case-study MRFs are developed considering sixteen configurations for each case characterised by different design parameters and structural properties. The parametric analysis provides a more comprehensive view of the assumptions and limitations of the design methodology and suggests additional recommendations to improve the design requirements of the SC-CB connections.

Keywords: Steel Moment Resisting Frames, Self-Centring Column Bases, Structural Resilience, Parametric Finite Element Analysis.

1 INTRODUCTION

Steel Moment Resisting Frames (MRFs) represent widely used seismic resisting systems in building structures, thanks to their architectural flexibility and good seismic performance [*e.g.,* 1-2]. For these structures, the traditional 'capacity design' philosophy currently implemented in modern seismic codes [*e.g.,* 3-5] ensures the achievement of adequate ductility and energy dissipation capacity, but it may entail the occurrence of irreparable damage of the structural components and large residual deformations in the aftermath of strong earthquakes [*e.g.*, 6]. This leads to high direct (*i.e.*, repair costs) and indirect (*i.e.*, business interruption) losses, which, in many cases, are not acceptable from both social and economic perspectives [*e.g.,* 7]. This situation strongly affects communities subjected to extreme seismic events, especially when damaged structures include strategic facilities that must remain operational in the aftermath of a damaging earthquake. In this direction, nowadays, earthquake engineering is facing an extraordinarily challenging era with the task of providing innovative seismic-resilient structures which are durable, efficient and capable of reducing direct and indirect losses after severe seismic events [*e.g.,* 8-13]. Examples of such structures are represented by Self-Centring MRFs (SC-MRFs) equipped with Post-Tensioned (PT) bars/strands, which provide elastic restoring forces, combined with replaceable/repairable energy dissipation devices [*e.g.,* 14-18].

It has been demonstrated that Column Bases (CBs) play a fundamental role over the self-centring capacity of MRFs. Conventional full-strength steel CBs suffer from residual rotations, large plastic deformations [*e.g.,* 19- 20], and axial shortening phenomena [*e.g.,* 21-22], which impair the structure returning to the initial condition after severe earthquakes. In fact, post-earthquake inspections after the 1994 Northridge, 1995 Kobe, and 2011 Tohoku earthquakes revealed unsatisfactory performances, confirming the susceptibility of CBs to difficult-to-repair damage and residual deformations due to several effects, such as anchor rods elongation, base plate yielding, weld fracture and concrete crushing [*e.g.,* 23-25]. Additionally, it is worth mentioning that the design assumptions for the CBs may significantly affect the seismic response of the structure. CBs can be designed as fully fixed, pinned, and other intermediate stiffness conditions (*i.e.*, rigid, flexible, semi-rigid). However, the stiffness and cyclic response of conventional CBs are difficult to predict, as they are strongly affected by the base plate flexibility and the magnitude of the axial force [*e.g.,* 26]. Several studies in this direction demonstrated that the assumptions made on the CBs' stiffness might underestimate or overestimate the height-wise distribution of steel MRFs' drift demands and the internal force distribution, thus leading to uneconomical or unconservative designs [*e.g.,* 27-29].

To overcome these drawbacks, in the last two decades, several research studies have proposed novel CB configurations. Several strategies focused on replacing the conventional full-strength CB connections with dissipative partial-strength joints equipped with Friction Devices (FDs) [*e.g.*, 30-31]. Among others, MacRae *et al.* 2009 [30] proposed a low-damage connection where the reduction of the column yielding, due to the introduction of the FDs, is identified as an effective solution to mitigate the axial shortening. Furthermore, other CBs configurations were developed combining self-centring systems and energy dissipation devices (*e.g.*, yielding or FDs) designed for easy inspection and replacement after strong seismic events [*e.g.*, 32-44]. Freddi *et al.* 2017 [38] presented and experimentally investigated [39] a rocking damage-free steel CB, which uses PT high-strength steel bars to control the rocking behaviour, FDs to dissipate the seismic energy, and a circular steel plate with rounded edges as a rocking base. A similar configuration was proposed by Kamperidis *et al.* 2018 [40] while using a square rocking base and hourglass shape steel yielding devices. Moreover, Wang *et al.* 2019 [41] experimentally and numerically examined two types of self-centring steel CBs composed of a concrete-filled square steel section, showing stable self-centring and energy dissipation capabilities. In addition, several studies also focused on achieving the self-centring behaviour using advanced materials (*i.e.*, super-elastic shape memory alloys) [*e.g.*, 43-44].

Within this context, Latour *et al.* 2019 [42] recently proposed and experimentally tested an innovative damage-free Self-Centring Column Base (SC-CB) consisting of a rocking column splice joint where a combination of FDs and PT bars with disk springs promote the self-centring behaviour of the connection. The damper typology included in this connection was extensively studied in previous experimental works, which have addressed significant aspects, such as the response of the FDs under cyclic loading histories and the behaviour of the pre-loadable bolts at installation and over their service-life [*e.g.*, 45-49]. Results from the experimental tests showed a satisfactory and stable flag-shaped hysteretic behaviour of the SC-CB. They also highlighted the influence of some design parameters over the joint response, such as the assumed design value of the axial load, as well as the key role of the initial pre-load of the PT bars on the self-centring response of the device. In this direction, the authors have recently investigated the global behaviour of the SC-CB using simplified numerical models, with the objective of evaluating the potentialities and limitations of the use of these joints in terms of residual drifts reduction within steel MRFs [50-51].

However, the parameters investigated in the experimental campaign were limited, and the previously proposed simplified numerical models highlighted some limitations in providing a more exhaustive view into the influence of some design parameters over the local behaviour of the connection. Thus, further research and additional information are still required towards the definition of pre-qualified design rules [*e.g.*, 52-55] for these joints. In this regard, it is of paramount importance to investigate the influence of the adopted design procedure over the global and local response of the SC-CBs, toward the objectives of obtaining the optimal design condition which provides the self-centring behaviour, as well as minimizing the yielding of the joint components. These considerations motivated the present research activity, whose main objectives are: *i)* to provide insights into the local behaviour of SC-CBs under cyclic loading; *ii)* to identify the parameters that mainly affect the local behaviour of SC-CBs in view of obtaining specific performance objectives (*i.e.*, minimal yielding of the joint components and self-centring capacity under random loading histories); *iii)* to propose new design guidelines for this joint typology.

To fulfil these objectives, a detailed Finite Element (FE) model is developed in ABAQUS [56] and validated against the available experimental results of the previously tested SC-CB specimen. The results of the FE validation show that the model correctly predicts the global hysteretic response observed during the experimental tests, providing useful insights into the characterization of the local behaviour of the SC-CB connection. A parametric FE analysis is conducted in ABAQUS [56], selecting three SC-CBs to investigate the scale effect on different geometrical configurations. The SC-CBs are extracted from three different case-study MRFs and are designed by following a proposed design procedure. Hence, a matrix of sixteen different configurations is considered for each SC-CB, obtained by varying three design properties of the joints. Global and local parameters are monitored and compared for each SC-CBs, considering all the configurations, to identify the best design solution in terms of improved self-centring capacity of the joint and minimal yielding of the components. The results of the FE parametric analysis provide more comprehensive insights on the assumptions and limitations of the design methodology and suggest additional recommendations to improve the design requirements.

The paper is organized as follows: Section 2 describes the main features and the behaviour of the SC-CB joint considered, highlighting the assumptions and limitations of the design methodology; Section 3 reviews an experimental study of a SC-CB prototype, describes the FE modelling strategy and the validation against the experimental results; Section 4 presents the design of three case study SC-CBs, describes the investigated sixteen configurations for each SC-CB and critically compares the results obtained by the parametric FE analysis.

2 SELF-CENTRING COLUMN BASE (SC-CB)

2.1 Main features

The SC-CB connection proposed and experimentally tested by Latour *et al.* [42] is shown in Figure 1. It consists of a column composed of two parts connected by a combination of FDs, which dissipate the seismic input energy through the alternate slippage of the surfaces in contact, and a self-centring system which, together with the gap opening mechanism, controls the re-centring behaviour of the connection. The FDs consist of properly coated steel friction shims and steel cover plates clamped with pre-loadable bolts. The self-centring system is composed of PT bars symmetrically placed with respect to the column's depth and arranged in series with a system of disk springs. The disk springs are arranged in series and in parallel, granting an ideal stiffness–resistance combination into the self-centring system. It is worth mentioning that the overall dimension of the connection is similar to the size of a traditional column splice, and it is characterised by the absence of interaction with the concrete foundation.

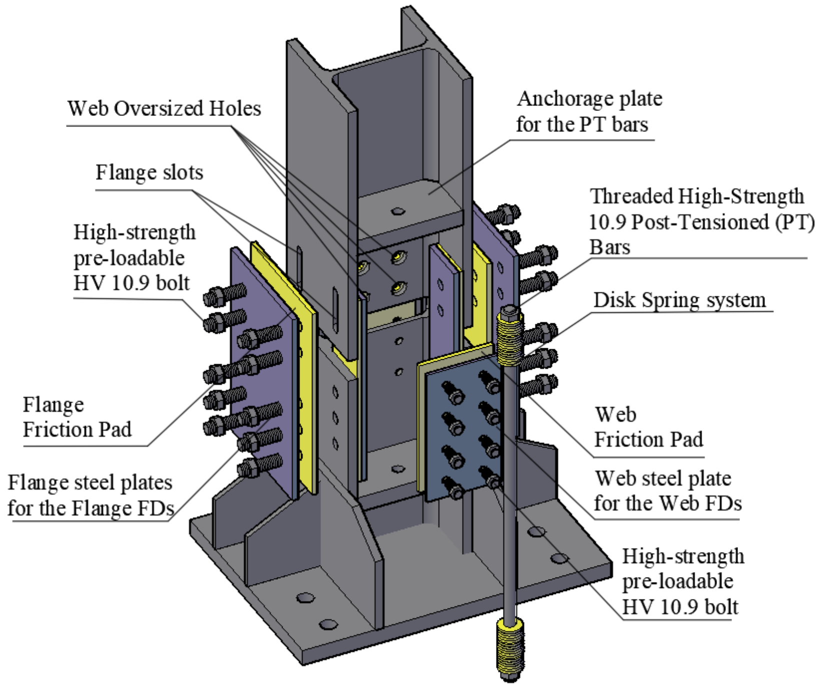

Figure 1: Self-Centring Column Base (SC-CB) experimentally tested in Latour et al. (2019) [42]

The design of the SC-CB joint is based on the knowledge of the forces developed during the gap-opening phase, as illustrated in Figure 2 (a). It is worth mentioning that some assumptions are required for the definition of the design formulations of the SC-CB joint. Some of these have been verified through experimental tests [42] and some others through simplified numerical models [50], nevertheless, there are some other assumptions which validity has not been verified yet.

The behaviour of the FDs assumes *i)* stable slippage force provided by the FDs, which is related to the stable friction coefficient and the clamping force of the bolts, which is assumed to be constant; and *ii)* negligible bending stiffness of the flanges' plates of the FDs. Based on these assumptions, the FDs exhibit a rigid-plastic behaviour that depends on the clamping force and the friction coefficient of the interfaces in contact. The forces in the FDs of the web (F_w) and flanges (F_f) are defined as follows:

$$F_w = F_{slip,w} = \mu \cdot n_s \cdot n_{b,w} \cdot F_{p,w} \qquad F_f = F_{slip,f} = \mu \cdot n_s \cdot n_{b,f} \cdot F_{p,f} \tag{1}$$

where μ is the design value of the friction coefficient; n_s is the number of friction interfaces (*i.e.*, equal to 2 in the considered configuration); $n_{b,w}$ and $n_{b,f}$ are the numbers of bolts respectively in the web and the flanges; $F_{p,w}$ and $F_{p,f}$ are the pre-loading forces of each web and flange bolt, respectively.

The PT bars control the rocking behaviour by providing elastic restoring forces in the joint. The force acting in the self-centring system (F_{PT}) (*i.e.*, PT bars and disk springs) is defined as follows:

$$F_{PT} = F_{PT,0} + \Delta F_{PT} \qquad F_{PT,0} = n_{PT} \cdot F_{p,PT} \qquad \Delta F_{PT} = K_{eq} \cdot \Delta l_{PT} \tag{2}$$

where $F_{PT,0}$ is the initial bars pre-load; ΔF_{PT} is the extra force occurring in the system during the gap opening phase, n_{PT} is the total number of PT bars employed; $F_{p,PT}$ is the initial pre-load force on each PT bar; K_{eq} is the stiffness of the self-centring system; Δl_{PT} is the average elongation of the PT bars, assumed linearly proportional to the target rotation (θ_t) of the joint, corresponding to 0.04 rads, which is the benchmark rotation established by AISC 341-16 [3] for Special MRFs. The equivalent stiffness of the self-centring system (K_{eq}) is a function of the stiffness of the single components (*i.e.*, PT bars and disk springs), as follow:

$$K_{eq} = n_{PT}\frac{K_{PT,1}K_{DS}}{K_{PT,1}+K_{DS}} \qquad K_{PT,1} = \frac{E_{PT}A_{s,res,PT}}{l_{PT}} \qquad K_{DS} = \frac{n_{ds,par}}{n_{ds,ser}}K_{ds,1} \tag{3}$$

where $K_{PT,1}$ is the stiffness of a single PT bar; K_{DS} is the stiffness of a set of disk springs arranged both in series and in parallel; E_{PT} is the elastic modulus of the PT bars; $A_{s,res,PT}$ is the resistance area of one PT bar; l_{PT} is the length of the PT bar (including the length of the disk spring system (l_{ds})); $K_{ds,1}$ is the stiffness of one disk spring, while $n_{ds,par}$ and $n_{ds,ser}$ are the number of disk springs arranged in parallel and series, respectively.

The SC-CB is characterised by a flag-shape moment-rotation behaviour as shown in Figure 2 (b). In the closed phase, the forces in the FDs are assumed to be completely developed and thus their contributions are assumed to remain constant during the gap opening. In addition, the contribution of the initial pre-load force of the PT bars is assumed constant, while the contribution due to the extra forces in the re-centring system (*i.e.*, occurring in the gap-opening phase) is assumed linearly proportional with the rotation of the joint. The moments' contributions are a function of the forces developed by each component during the gap-opening phase and can be calculated, with respect to the Centre of Rotation (COR), as follow:

$$M_D = M_N + M_{PT,0} \qquad M_N = N_{Ed}\cdot(z/2) \qquad M_{PT,0} = F_{PT,0}\cdot(z/2) \tag{4}$$

$$M_{FD} = M_{FD,w} + M_{FD,f} = F_w\cdot(z/2) + F_f\cdot z \tag{5}$$

$$\Delta M_{PT} = \Delta F_{PT}\cdot(z/2) = K_{eq}\theta_{joint}\cdot(z/2)^2 \tag{6}$$

where M_D is the decompression moment; M_{FD} is the moment provided by the web and flanges FDs; ΔM_{PT} is the moment developed by the additional forces in the self-centring system; θ_{joint} is the rotation of the joint, and z is the lever arm of the connection. The first branch (K_1) of the moment-rotation curve is characterized by an infinite stiffness of the connection and, therefore, the stiffness of the whole system is equal to the flexural stiffness of the cantilever column. The second branch (K_2) is controlled by the equivalent stiffness of the self-centring system (K_{eq}). It is worth reminding that the flexural resistance of the flange cover plates and friction shims is assumed negligible, thus their bending contribution on the moment-rotation behaviour is neglected. Further investigations are reported in Section 4.3.

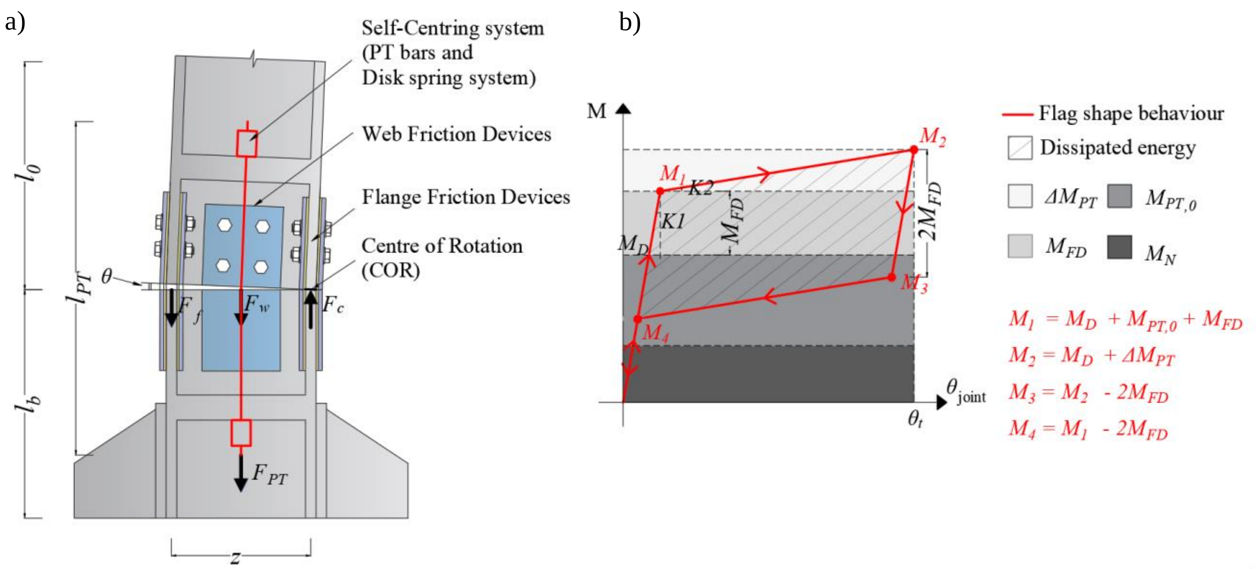

Figure 2: Self-Centring Column Base (SC-CB): (a) Schematic representation during the gap-opening; (b) Flag-shape hysteretic behaviour, moment contributions.

2.2 Design procedure

The design of the SC-CB is based on a step-by-step procedure consisting of the definition of the design input parameters (*i.e.*, geometry and design forces in the column), the design of the components (*i.e.*, FDs and Self-centring system) and the design of the structural details of the joint (*i.e.*, plates of the FDs, holes and slots). The design methodology is affected by the assumptions previously discussed in Section 2.1. Additionally, some design choices are required, such as: *i)* the design axial force assumed to be constant considering two limit conditions; *ii)* the design shear force assumed to be entrusted to the web FDs; *iii)* no yielding of the joint components. However, currently, there are no recommendations that allow identifying the optimal design condition in terms of self-centring behaviour and minimal yielding of the components, and some advancements in this direction are provided in this paper. Further considerations on the design assumptions and limitations are reported in the subsequent sections.

Step 1: Design input parameters

The design procedure of the SC-CB requires as input parameters: *i)* the geometrical properties of the column (*i.e.*, cross-section properties and the splice position above the foundation (l_b)); *ii)* the design forces in the column (*i.e.*, the maximum/minimum expected axial forces ($N_{Ed,max}$;$N_{Ed,min}$) and the design bending moment (M_{Ed})) derived through the procedure suggested by the Eurocode 8 [1], namely considering a proper overstrength of the dissipative zones.

The design shear force in the column base joint is estimated as:

$$V_{Ed} = M_{Ed}/l_0 \tag{7}$$

where $l_0 = l_s - l_b$ with l_s and l_b being respectively the column shear length and the distance between the spliced section and the base.

Once selected the input parameters, the design of the SC-CB connection can be addressed by first designing the bolts of the web FD and, consequently, designing the PT bars and the bolts of the flange FDs. Two primary checks must be satisfied: *i)* no yielding of the column; *ii)* self-centring behaviour. These conditions are summarised in the following system of inequalities:

$$\begin{cases} M_2 < M_{y,c} \\ M_D \geq M_{FD} \end{cases} \tag{8}$$

where M_2 is the moment achieved at the maximum rotation, and $M_{y,c}$ is the column's yielding bending moment.

Regarding the design axial force (N_{Ed}), it is worth highlighting that the adoption of a constant axial force is clearly not reproducing the real load situation of all the columns of a MRF, due to large axial force fluctuations that happen during the earthquake. Generally, the axial force in the columns of a MRF varies according to *i)* the distribution of the gravity loads; *ii)* the force fluctuations during the earthquake loading. In fact, especially the external columns usually experience significant transient axial load demands, due to the dynamic overturning effects of the earthquake. Conversely, the internal columns typically undergo lower axial load fluctuations during the seismic event.

Therefore, in order to properly account for the variability of the axial force within the design procedure, the maximum compressive ($N_{Ed.max}$) and the minimum compressive (maximum tensile) ($N_{Ed,min}$) axial forces are considered. Therefore, the initial sizing of the SC-CB is performed considering the maximum axial force, which represents the worst condition for the no yielding requirement (*i.e.*, first check condition of Eq. (8)) and the design is successively verified considering the minimum axial force, which is the worst condition for the self-centring requirement (*i.e.*, second check condition of Eq. (8)). Nevertheless, designing with the min compressive axial force may represent an overconservative design assumption, which may lead to an overestimation/oversizing of the necessary components of the self-centring system. Further explanations and considerations on the validity of these assumptions are reported in Section 4.5

Step 2: Design of the components

The web FD is assumed to carry alone the design shear load (V_{Ed}). Therefore, the required pre-load force for each web bolt ($F_{p,w}$) is easily determined by imposing that the slippage force of the web FD (F_w) (see Eq. (1)) must be larger or equal to the required value of the design shear force (V_{Ed}) (see Eq. (7)), as follow:

$$F_w = \mu \cdot n_s \cdot n_{b,w} \cdot F_{p,w} \geq V_{Ed} \quad \rightarrow \quad F_{p,w} \geq \frac{V_{Ed}}{\mu \cdot n_s \cdot n_{b,w}} \tag{9}$$

Additional information and details regarding this design assumption are further investigated in Section 4.4.

The post-tensioning force of the PT bars (F_{PT}) is defined by imposing the system of equations for the self-centring condition of Eq. (8) and the equilibrium between the internal and external bending moment in the SC-CB, as follows:

$$\begin{cases} F_{PT} \geq 2F_f + F_w - N_{Ed} \\ F_{PT} \cdot (z/2) + F_f\,(z) = M_{Ed} - (F_w + N_{Ed})(z/2) \end{cases} \rightarrow \quad F_{PT} \geq \frac{M_{Ed}}{z} - N_{Ed} \tag{10}$$

In addition, the minimum pre-load force for each flange bolt ($F_{p,f}$) is provided by addressing the contribution of the force of the PT bars and the force of the web FD. The slippage force of the flange FDs (F_f) (see Eq. (1)) can be obtained by Eq. (10) as indicated by the following expressions:

$$F_f = \frac{M_{Ed}}{z} - \frac{1}{2}(F_w + N_{Ed} + F_{PT}) \;\rightarrow\; F_{p,f} = \frac{F_f}{\mu \cdot n_s \cdot n_{b,f}} \tag{11}$$

The number of disk springs in parallel ($n_{ds,par}$) is calibrated to control the yielding resistance of the re-centring system while the number of disk springs in series ($n_{ds,ser}$) controls the stiffness of the self-centring system (see Eq. (3)).

Step 3: Design of the structural details

Anchorage plates for the PT bars are placed symmetrically along with the column's depth and welded to the column, as shown in Figure 3 (a). The dimensions of the plates are known (*i.e.*, b_p and l_p), except for the thickness (t_p), which is designed to resist the total force of the PT bars (F_{PT}) (see Eq. (1)).

The flange cover plates the flange FDs are designed and verified to resist the tensile force provided by the design actions (*i.e.*, the contribution of M_{Ed}, N_{Ed}, F_w and F_{PT}). It is worth highlighting that the contribution of the friction shims to the tensile resistance of the FDs is neglected, as well as the flexural resistance of the flange cover plates and friction shims, as previously discussed. More details and investigations regarding the validity of the assumptions for the flanges' plates are further checked through the parametric numerical analysis in Section 4.3.

Web oversized holes (d_h) and flange slots (l_{slot}) are designed to accommodate the design rotation (θ_t) during the gap opening phase, as illustrated in Figure 3 (b). The holes' positions are designed to comply with the edge distances and spacing of bolts suggested by Eurocode 3 Part 1-8 [57]. Finally, the design resistance of the lower part of the connection is calculated and checked, considering the failure modes (*i.e.*, shear resistance, bearing resistance, punching shear resistance, combined shear and tension) as indicated in the Eurocode 3 Part 1-8 [57].

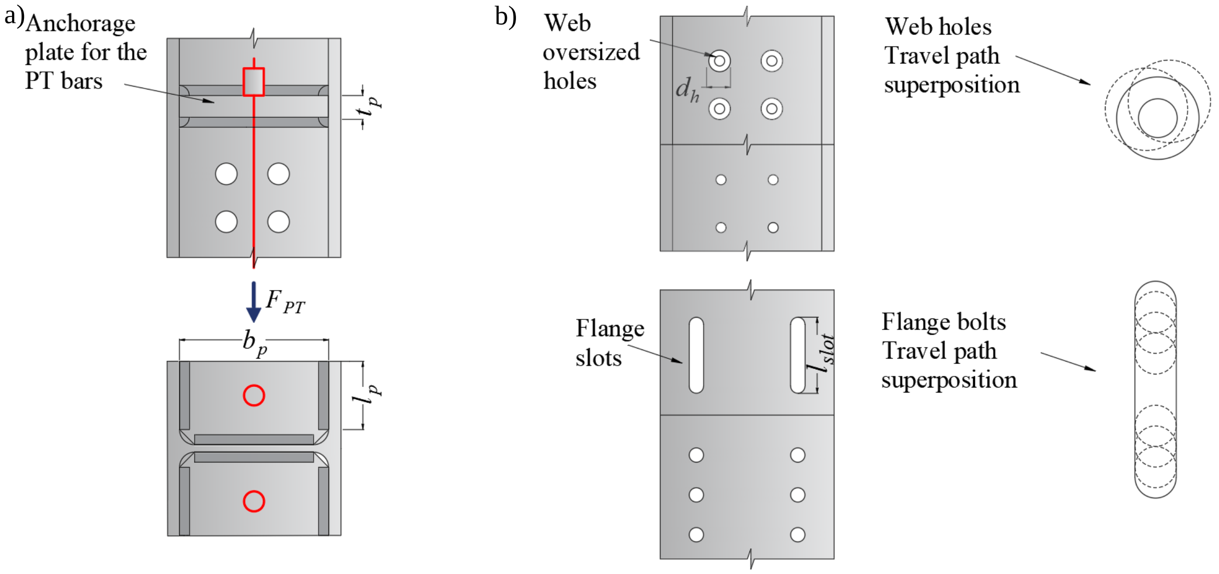

Figure 3: Structural details: a) Anchorage plate for the PT bars; b) Plates of the FDs; c) Oversized holes and slots.

3 FINITE ELEMENT MODELLING AND VALIDATION

The experimental campaign of the SC-CB performed by Latour *et al.* [42] is briefly summarized hereafter. Subsequently, the advanced FE model in ABAQUS of the SC-CB is described and validated against the experimental results. The FE model allows evaluating the significant parameters affecting the moment-rotation hysteretic behaviour of the SC-CB while allowing shedding some light on the critical aspects of the design procedure presented in Section 2.

3.1 Review of the experimental campaign

The experimental campaign focused on an isolated full-scale column with the SC-CB connection and consisted of several quasi-static cyclic tests. The key characteristics of the test and the main results are briefly summarized herein to investigate the validation process.

Figure 4 (a) shows a detail of the specimen considered within the experimental campaign. This consists of a HE 240B column of S275 steel class, where the FDs were made of 8 mm coated friction shims and cover plates of 5 mm and 8 mm for the web and the flanges, respectively. All the plates were S275 steel class, and the bolts were high-strength pre-loadable HV 10.9 class. The friction interface was characterised by a friction coefficient (μ) assumed equal to 0.53 according to previous experimental studies [45-47]. Besides, the self-centring system was composed of two threaded high-strength M20 PT bars of 10.9 class, and the disk springs system consisted of Belleville Disk Springs DIN 6796 arranged with three disks in parallel and seven disks in series. The anchorage plates were made of 40 mm S275 steel plates welded to the inner parts of the column. An overview of the tested specimen, containing the dimensions of the spare components, is illustrated in Figure 5.

The main material properties of the joint components are summarized in Table 1, where E, f_y and f_u are the nominal values of the Young's modulus, the yield strength and ultimate tensile strength of the materials, respectively. The other proprieties of the adopted structural steel (*i.e.*, the shear modulus, the Poisson's ratio and the coefficient of linear thermal expansion) are based on the Eurocode 3 Part 1-1 [58]. The interested reader can find additional information in Latour *et al.* 2019 [42]. In this paper, the results of three cyclic tests are selected and used to validate the FE model, as explained in the subsequent section.

The testing equipment is shown in Figure 4 (b). The loads in the quasi-static tests have been applied through two hydraulic actuators. One actuator is used to apply the axial force, which is kept constant during the test, while a horizontal hydraulic actuator is used to impose a horizontal cyclic displacements history with an increasing amplitude at each step, consistently with the loading protocol suggested by AISC 360-10 (Figure 6). It is important to underline that, although the adoption of a constant axial force is not fully representative of a real situation in a steel MRF, this assumption allowed an easier interpretation of the experimental results. Several cyclic tests were performed varying some design parameters (*i.e.*, the axial load in the column, the pre-loading force in the bolts of the FDs, the pre-loading force in the PT bars) to evaluate their influence on the overall experimental response of the joint. It is noteworthy that axial load ratios equal to 25% (*i.e.*, 728 kN) and 12.5% (*i.e.*, 350 kN) have been selected in a reasonable range of variation, considering the typical size of MRFs designed according to Eurocode 8 [3].

The pre-loading forces of the bolts and the bars were applied with a calibrated torque wrench, while four load cells were installed in the connection to monitor the tensile forces of the PT bars and in two bolts of the flange FDs, as shown in Figure 4 (c). In addition, LVDT displacement transducers have been adopted to measure the vertical displacements in both column sides. Regarding the bolt tightening procedure, it is worth mentioning that the initial pre-load of the bolts, according to EN 1090-2 [59] specifications, was increased by 10% to account for random variability of the bolt tightening and initial installation loss.

Table 1: Material properties [42].

Elements	Class [-]	E [GPa]	f_y [MPa]	f_u [MPa]	Number [-]	Diameter [-]
Column and plates	S275	210	275	430	-	-
Web Bolts	HV 10.9	210	900	1000	4	M14
Flange Bolts	HV 10.9	210	900	1000	4	M20
PT bars	10.9	205	900	1000	2	M20

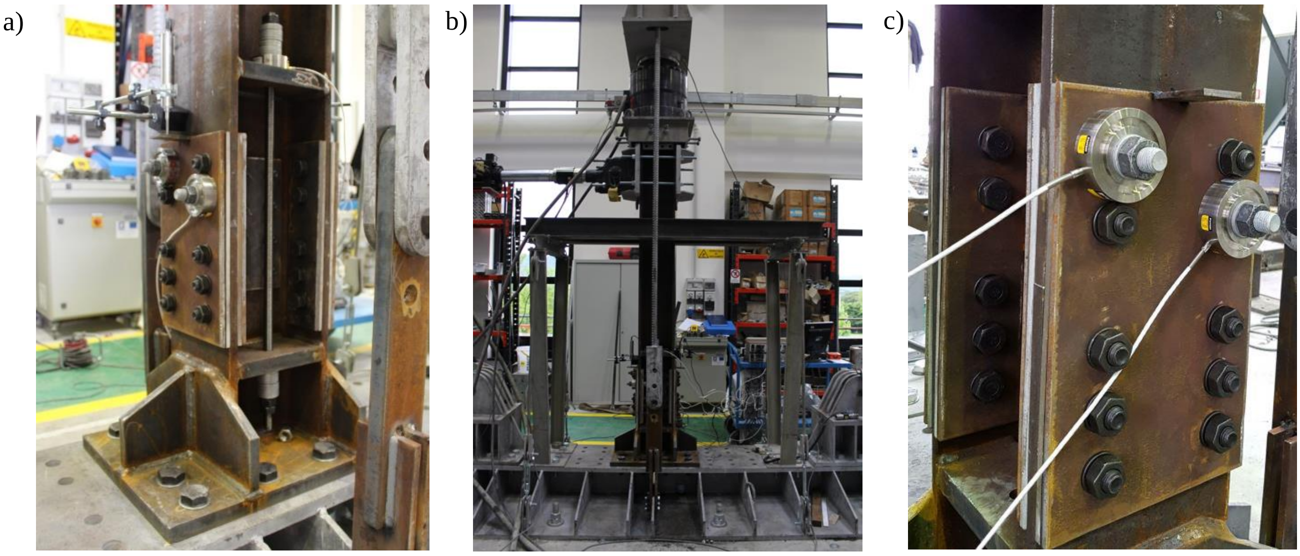

Figure 4: Experimental test of the SC-CB: a) Specimen; b) Test Set-Up; c) Details of the measurement devices.

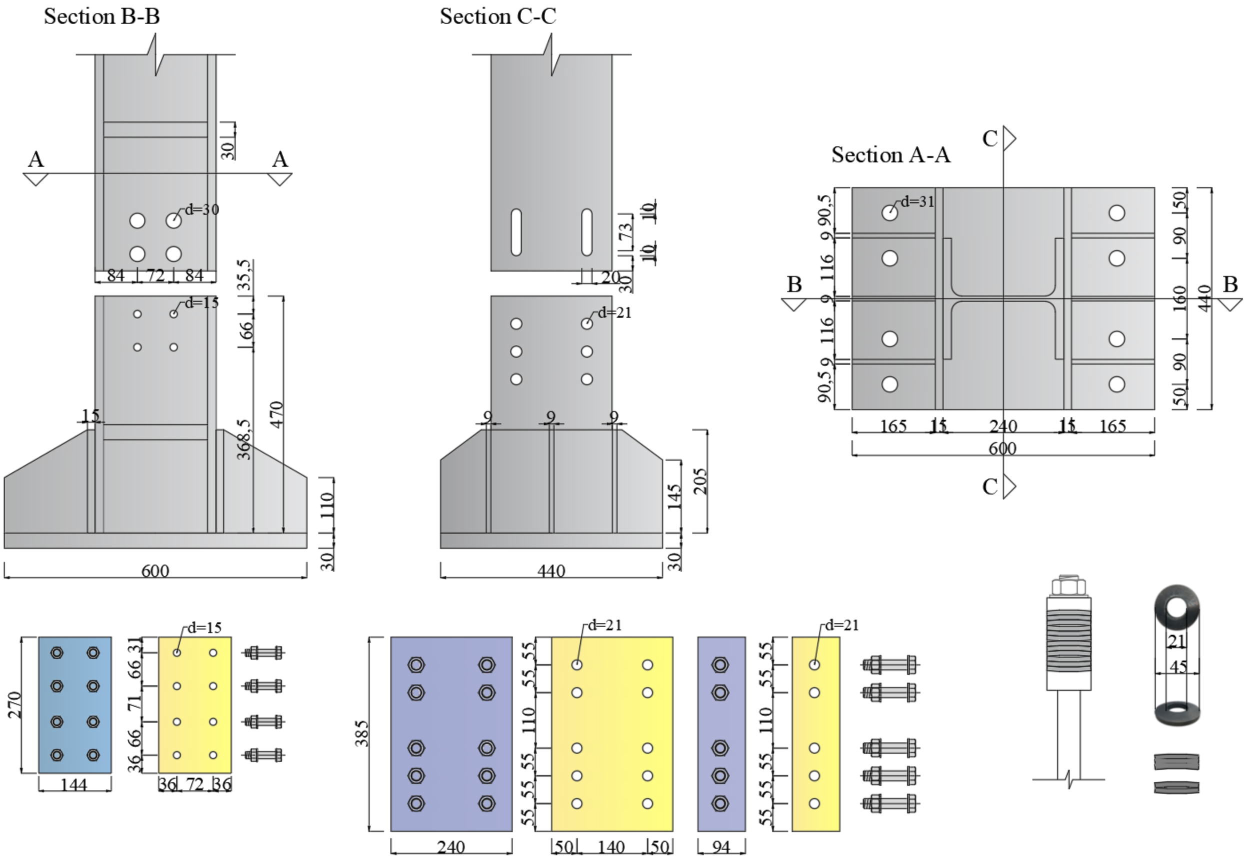

Figure 5: Geometry of the tested specimen SC-CB (dimensions in mm) [42].

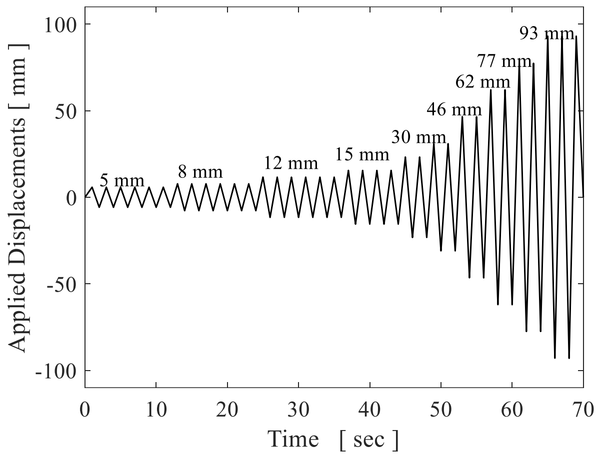

Figure 6: Experimental cyclic displacement loading history.

3.2 Modelling assumptions

An overview of the ABAQUS [56] model is shown in Figure 7. It is a detailed 3D non-linear FE model where the bottom surface of the base is fully fixed using boundary conditions type '*encastre*', while the lateral load of the horizontal actuator is simulated by a controlled horizontal displacement using boundary conditions type '*displacement*' (*i.e.,* U1=0, U2=1, UR3=0). Additionally, the gravity load is simulated by a uniform pressure applied at the upper surface of the column's cross-section to simulate the actuator. Figure 7 (a) shows the boundary conditions of the model.

All the components are modelled using the eight-node linear brick element (C3D8R) available in the ABAQUS library [56]. Elements C3D8R rely on '*reduced integration*' and '*hourglass control*', and meshing is carried out by selecting local seeds with mesh size 10 in the areas with contact interaction to monitor the complex stress distributions during the cyclic loading. Conversely, a mesh size 20 is used in the areas where the expected stresses are relatively insignificant (*i.e.*, the base and the upper part of the column). The curvature control is chosen with a maximum deviation factor of 0.1, while the minimum size control is specified equal to 0.1. Both geometrical and mechanical nonlinearities are considered. An overview of the mesh details is illustrated in Figure 7 (b), while the actual material properties are reported in Table 1. It is worth mentioning that a multilinear stress-strain law is exploited to model the mechanical properties of the steel, complying with the model proposed by Faella *et al.* 2000 [2].

The interaction properties among the parts are modelled with the '*surface-to-surface*' contact interaction. This is implemented using the '*hard*' contact property to describe the behaviour in the normal direction. In contrast, the '*penalty*' option is used for the tangential response with values of the friction coefficient equal to 0.30 for interfaces among steel parts (*i.e.*, plates, column, bolts, and PT bars) and 0.53 for the shims-steel interfaces of the FDs (*i.e.*, equivalent to the 5% dynamic percentile of the friction coefficient [45]). The options '*adjust only to remove overclosure*' and '*specify tolerance for adjustment zone*' are employed to overcome convergence problems associated with the non-linear nature of the contact regions of bolts and PT bars. The tolerance factor for the adjustment zone has been calibrated iteratively to provide adequate accuracy of the results while ensuring convergence. The '*TIE*' constraint is used to simulate full penetration welds (*i.e.*, monolithic connection) between the anchorage plates of the PT bars and the internal part of the column. Figure 7 (c) illustrates a detail of the spliced section with the contact interactions.

The option '*bolt load*' is used to model the initial pre-load force in the web and flange bolts and to model the initial post-tensioning force in the PT bars. The '*apply force*' option is used for bolts to keep the force constant throughout the analysis. Conversely, the '*adjust length*' option is used to allow correctly capturing the force variation of the PT bars (*i.e.*, elongation or shortening during the rocking behaviour). It is important highlighting that the self-centring system is modelled with only the PT bars, assigning the whole stiffness of the system composed of PT bars and disk springs. The '*von Mises yield criterion*' coupled with '*isotropic hardening*' is used to model plasticity. The analyses are performed considering three loading steps: *i)* application of the axial load; *ii)* bolts pre-loading; and *iii)* displacement history application. The displacement-controlled load protocol up to 93 mm (*i.e.*, joint rotation of 0.06 rad) is applied, consistently with the test procedure (Figure 6). The non-linear equilibrium equations are solved using the '*static general*' analysis procedure. The standard '*full Newton*' solution technique is adopted together with an automatic incrementation scheme for the application of the loading. The initial increment size is 0.001, while the minimum is 10^{-15}, and the maximum is 1. The '*automatic stabilization*' with '*specify dissipated energy fraction*' and with '*specify damping factor*' are adopted to overcome convergence problems during the analysis.

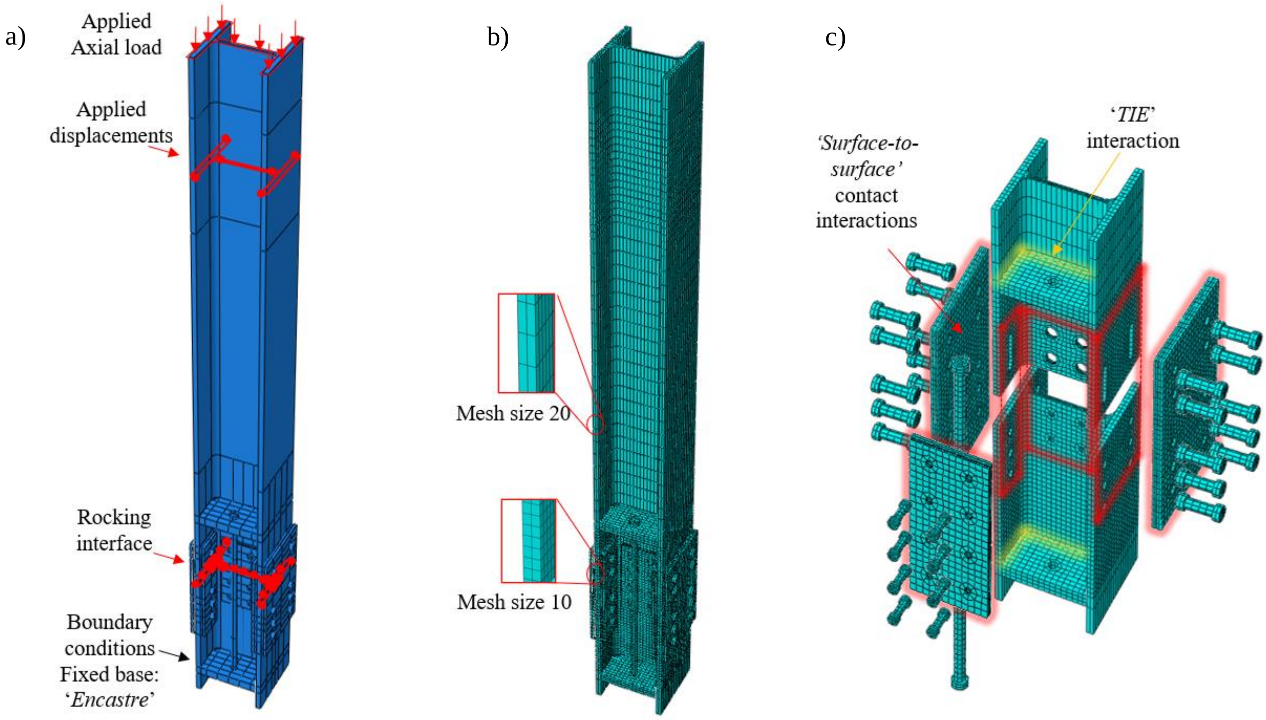

Figure 7: Overview of the finite element (FE) model of the SC-CB developed in ABAQUS [56]: a) Boundary conditions; b) Meshing details of the components; c) Interactions among the parts.

3.3 Validation

The FE modelling strategy is validated against the experimental results from Latour *et al.* [42] for three cyclic tests whose main design parameters (*i.e.*, the axial load in the column, the pre-loading force in the bolts of the FDs, the pre-loading forces in the PT bars) are reported in Table 2. Hence, FE models have been built in the ABAQUS [56], varying the aforementioned input parameters. Tests 1 and 2 are characterized by the higher value of the axial load (*i.e.*, 728 kN) and are performed respectively with and without the contribution of the PT bars. Test 3 is carried out considering the lower value of the axial load ratio (*i.e.*, 350 kN), and it is characterized by the absence of the contribution of the PT bars.

Table 2: Experimental input data [42].

Test	Axial load [kN]	Pre-load of each web bolt [kN]	Pre-load of each flange bolt [kN]	Pre-load in each PT bar [kN]
1	728	32	62	100
2	728	32	100	-
3	350	32	100	-

Figure 8 shows the comparison between the FE model and the experimental results in terms of moment-rotation (*M*-θ_{joint}) behaviour of the joints. The ABAQUS results are shown in red lines, while the experimental data are reported in blue lines. Also, the analytical moment-rotation relationships are reported with dotted black lines. The comparison shows a good agreement, demonstrating the effectiveness of the FE model and of the analytical formulation in predicting the experimental response. Figure 8 (a) (*i.e.*, high axial force and PT bars) shows a full self-centring behaviour with a very low residual rotation (*i.e.*, 2.1 mrad), Figure 8 (b) (*i.e.*, high axial force and no PT bars) shows a reduced self-centring capacity, while Figure 8 (c) (*i.e.*, low axial force and no PT bars) shows a significant residual rotation. These results highlight the influence of the axial force (N_{Ed}) and pre-load of the PT bars in controlling the moment-rotation behaviour of the SC-CB and demonstrate the ability of the numerical and analytical models in capturing these effects.

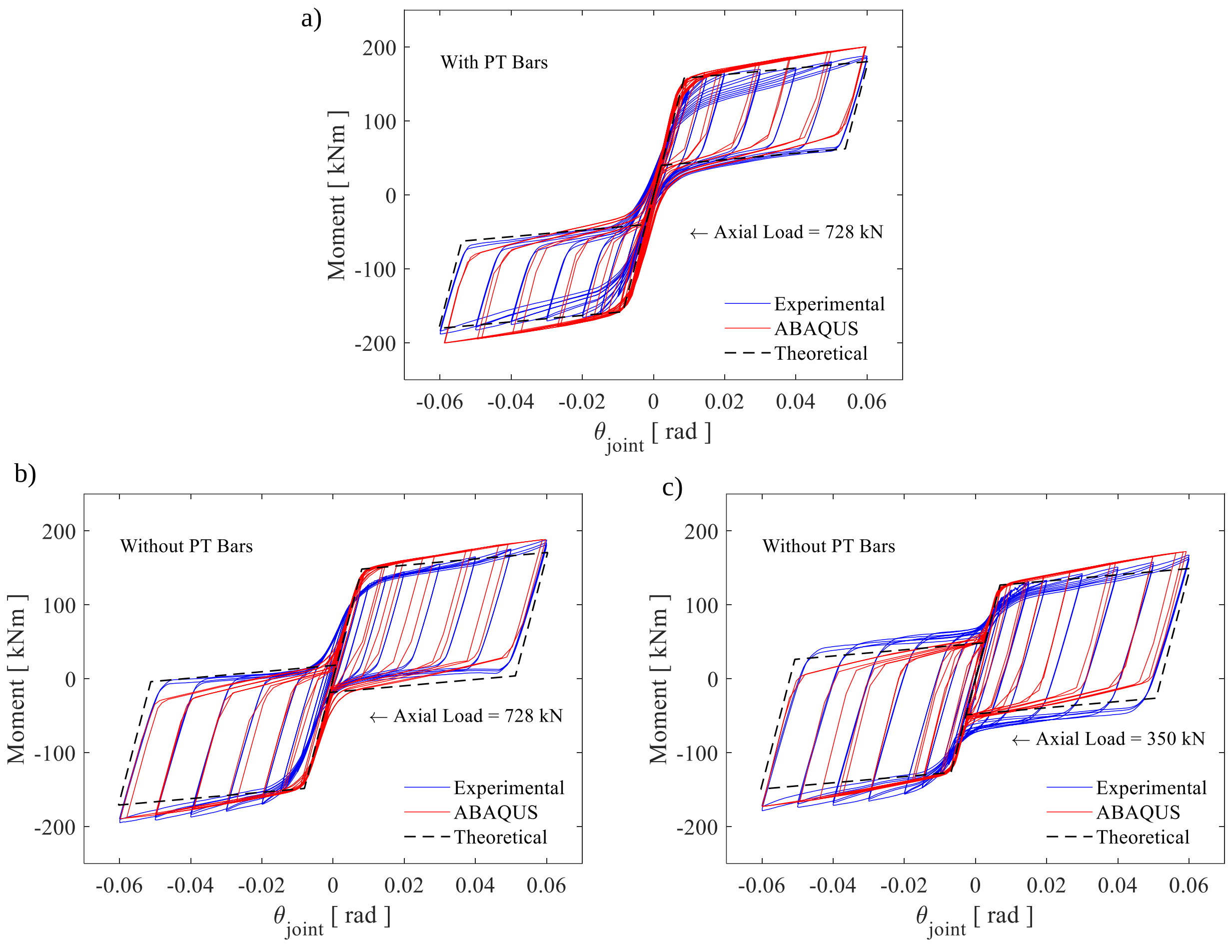

Figure 8: Comparison between FE models and experimental results [42]. Moment-Rotation hysteretic behaviour for the: a) Test 1; b) Test 2; c) Test 3.

Some limitations of the numerical and analytical models can be observed. Among others, as previously discussed, the analytical model neglects the flange plates' bending contribution, and the effect of this assumption is reflected in the slightly lower strain hardening behaviour of the analytical model with respect to both the experimental results and the ABAQUS model. Moreover, the experimental results showed a loss of the pre-loading force in the bolts of the FDs during the cyclic loading history. In particular, it has been noted that flange bolts, which were initially tightened to reach the proof load, were characterized by a loss of 7-10% of the initial pre-load after the first cycle of the loading history. Afterwards, they uniformly reached a total loss of about 20%. Also, the deterioration of the coating may represent a possible explanation for this loss. For these reasons, the web and flange bolts' pre-loading forces in the ABAQUS model were reduced by 20% with respect to the pre-loading experimental values. However, it is worth mentioning that the time history of the bolts' force loss is not simulated in the ABAQUS model, leading to some small differences between the numerical and experimental results.

4 PARAMETRIC FINITE ELEMENT ANALYSIS

A parametric FE analysis is carried out on three SC-CBs belonging to three different MRFs. The SC-CBs are designed by following the design procedure proposed in Section 2 and successively developed in ABAQUS following the modelling strategy discussed in Section 3. The objectives of the FE parametric analysis are *i)* to investigate the scale effect on different geometrical configurations of the SC-CB joint; and *ii)* to focus the attention on three crucial aspects deriving from the design assumptions, in view of obtaining specific performance objectives (*i.e.*, minimal yielding of the joint components and self-centring capacity).

4.1 Design of prototype SC-CBs from case study MRFs

The selected case-study MRFs are extracted from prototype structures equipped with perimeter MRFs located in the -*x* and *y*-directions, while the interior part is composed of gravity frames. The plans and the elevation views of the case-study MRFs are shown in Figure 9 (a) and (b), respectively. The present study focuses on the MRFs located in the *x*-direction, and the design is performed in accordance with the Eurocode 8 provisions [1]. The steel-concrete composite floor system is formed of steel beams and HI BOND A55/P600 type composite floor connected through shear connectors to a concrete slab. The gravity loads and the masses have been assessed considering the tributary areas depicted in Figure 9 (a) and evaluated based on the seismic combination of the Eurocode 8 [1]. The ULS (*i.e.*, Ultimate Limit State, probability of exceedance of 10% in 50 years) is defined considering the Type 1 elastic response spectrum with a peak ground acceleration equal to 0.35g and soil type C. The behaviour factor is evaluated according to the requirements of the Eurocode 8 [1] for MRFs in DCH and hence assumed as q = 6.5. The structures have non-structural elements fixed in a way so as not to interfere with structural deformations. Therefore, the interstorey drift limit for DLS (*i.e.*, Damage Limit State, probability of exceedance of 10% in 10 years) is assumed as 1%, accordingly to Eurocode 8 [1] recommendations. The indications of the beams and columns cross sections are reported in Figure 9 (b). Two steel grades are used for the beams and the columns: the steel yield strength is equal to 355 MPa for columns and 275 MPa for beams. The fundamental periods of vibration are respectively equal to T_1 = 0.45, 0.56 and 0.74 sec for the MRF1, MRF2 and MRF3.

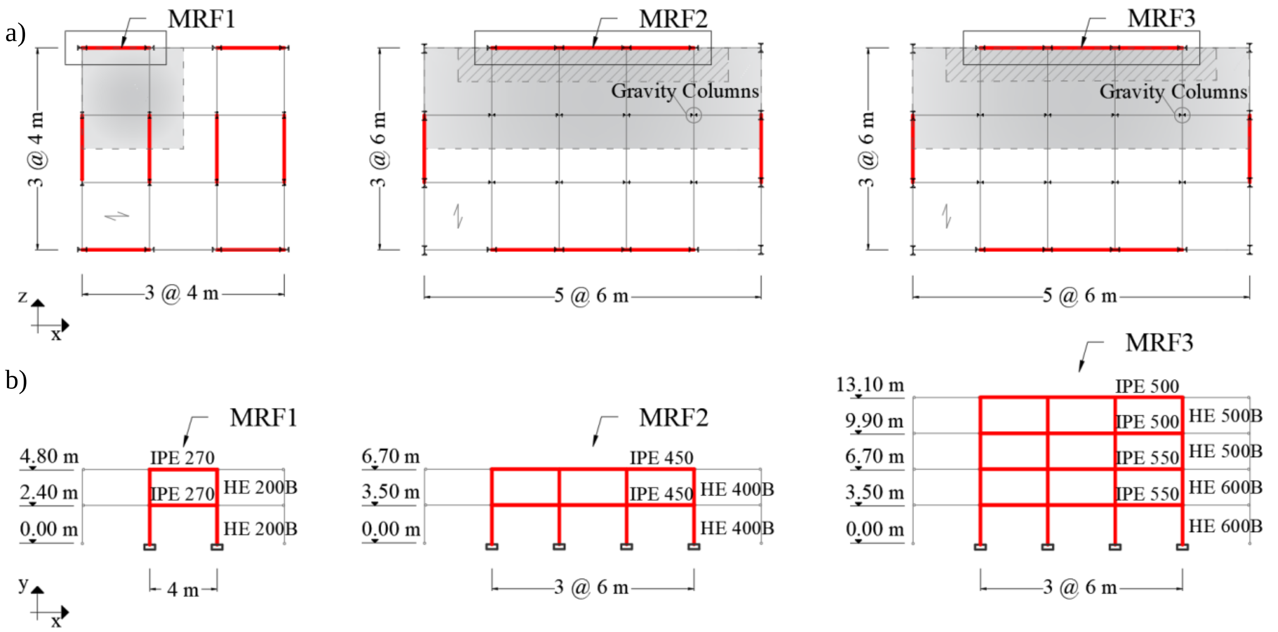

Figure 9: Case-study buildings: a) Plan views; b) Elevation views.

The cross-section profiles of the first storey external columns are respectively HE 200B, HE 400B, and HE 600B of S355 steel class. The geometrical configurations of the SC-CBs are indicated in Table 3, including the position of the spliced sections and the internal lever arm for each connection. The three considered SC-CBs are hereinafter referred to as SC-CB1, SC-CB2 and SC-CB3. The design input actions are reported in Table 4, where "–" stands for tension and "+" for compression. It is worth mentioning that these columns actions are defined by considering the proper location of the spliced sections. The FDs are composed of 8 mm coated friction shims of S355 steel class, clamped with HV 10.9 class bolts and S355 steel cover plates for both web and flanges. The geometry and the structural details of the web and flanges FDs are reported in Table 5 and Table 6, respectively. The friction coefficient (μ) is assumed equal to 0.53 consistently with previous studies [45-47]. The self-centring system includes high-strength PT bars 10.9 class and disk springs special washers DIN 6796, whose properties are indicated in Table 7. It is important to mention that the indications of the pre-loading forces refer to each bolt or PT bar, and the symbology used for Table 3 - Table 7 is consistent with that reported in the design formulations (see Section 2).

Table 3: SC-CBs geometrical configurations

Specimen	Column [-]	Spliced section [mm]	Internal lever arm *(z)* [mm]
SC-CB1	HE 200B	500	185
SC-CB2	HE 400B	700	374
SC-CB3	HE 600B	850	570

Table 4: SC-CBs Design input actions

Specimen	N_{Ed} [kN]	M_{Ed} [kNm]	V_{Ed} [kN]
SC-CB1	+138, -127	127	115
SC-CB2	+372, -183	683	427
SC-CB3	+400, -807	1430	765

Note: negative values are for tension; positive values are for compression.

Table 5: Web FDs geometry and structural properties

Specimen	b_{wp} [mm]	h_{wp} [mm]	t_{wp} [mm]	$e1$ [mm]	$p1$ [mm]	$e2$ [mm]	$p2$ [mm]	d_h [mm]	$z/2$ [mm]	Bolts [-]	$n_{b,w}$ [-]	$F_{p,w}$ [kN]
SC-CB1	130	300	8	30	70	30	70	30	93	M14	4	28
SC-CB2	290	600	12	80	140	75	140	60	187	M27	4	100
SC-CB3	390	800	15	120	180	90	200	75	258	M30	4	181

Table 6: Flange FDs geometry and structural properties

Specimen	b_{fp} [mm]	h_{fp} [mm]	t_{fp} [mm]	$e1$ [mm]	$p1$ [mm]	$e2$ [mm]	$p2$ [mm]	l_{slot} [mm]	z [mm]	Bolts [-]	$n_{b,f}$ [-]	$F_{p,f}$ [kN]
SC-CB1	200	300	8	50	50	39	122	30	185	M14	4	34
SC-CB2	400	600	12	80	70	60	184	60	374	M27	6	44
SC-CB3	600	800	15	100	100	65	170	75	570	M27	6	68

Table 7: Self-centring system geometry and structural properties

Specimen	t_p [mm]	Bars [-]	n_{PT} [-]	$F_{p,PT}$ [kN]	n_{par} [-]	n_{ser} [-]	K_{PT} [kN/mm]	K_{DS} [kN/mm]	K_{eq} [kN/mm]	Δl_{PT} [mm]
SC-CB1	40	M30	2	366	3	7	162	39	63	4
SC-CB2	85	M36	4	514	4	18	112	21	69	13
SC-CB3	100	M36	6	514	4	26	84	14	72	18

4.2 Investigated parameters and methodology

The parametric FE analysis focuses on three crucial aspects deriving from the design assumptions, which can be summarized as follow: *i)* the bending contribution of the flanges' plates; *ii)* the definition of the distribution of the shear forces among the components; *iii)* the effect of the axial design force over the self-centring capacity/damage in the components. Therefore, three design parameters of the SC-CB joints are selected: *i)* the thickness of the flanges' plates; *ii)* the percentage of the design shear force to be entrusted to the web FDs in the design phase; *iii)* the axial load variability. Subsequently, a matrix of sixteen design configurations is considered for each SC-CB, obtained by varying the aforementioned design parameters. An overview of the configurations for each SC-CB is indicated in Table 8.

The thickness of the flange plates is selected to be varied by considering two limit configurations for each SC-CB. The first corresponds to the design thickness (*i.e.*, obtained as the lower limit with respect to the axial force transmitted by the flange plates), while the second one refers to a value two times larger. It is important to remind that the design assumptions for the flanges' plates are indicated in Section 2.

Additionally, the design shear load percentage which is considered to be entrusted to the web FDs in the design phase is assumed to be varied in a range of cases (*i.e.*, 100%, 75%, 50%, 0% of the total shear force (V_{Ed})). These configurations are hereinafter referred to as 100%, 75%, 50% and 0%WFD, where 50%WFD indicates that 50% of the total shear force is entrusted to the web FDs. This parameter is investigated to provide information on how this design choice affects both global and local behaviour of the SC-CB connection while evaluating the corresponding mechanism of the shear redistribution among the different joint components (*i.e.*, the web FDs, the flange FDs, the PT bars and the sliding mechanisms of the friction at the rocking interface).

Each configuration is analysed when subjected to the maximum and minimum design axial load in order to evaluate the influence of the axial load variability over the global and local response. Moreover, in order to verify the validity of the design assumptions concerning the design axial load described in Section 2, an additional design configuration of the SC-CB is developed and analysed, obtained by assuming the axial load due to the gravity loads as the design axial load. Further explanations are given in Section 4.5.

Table 8: Matrix parameters for each SC-CB

Model	Flanges' Plates Thickness	Shear Load % Web FDs	Axial Load
Configuration 1	$t_{p,f}$	100	Max (+)-Min (-)
Configuration 2	2 t_{fp}	100	Max (+)-Min (-)
Configuration 3	t_{fp}	75	Max (+)-Min (-)
Configuration 4	t_{fp}	50	Max (+)-Min (-)
Configuration 5	t_{fp}	0	Max (+)-Min (-)
Configuration 6	2 t_{fp}	75	Max (+)-Min (-)
Configuration 7	2 t_{fp}	50	Max (+)-Min (-)
Configuration 8	2 t_{fp}	0	Max (+)-Min (-)

FE models of the three SC-CBs are developed in ABAQUS [56] by following the validated methodology defined in Section 3. An overview of the three FE models is shown in Figure 10. Sixteen static cyclic analyses are performed for each SC-CB, imposing a horizontal cyclic displacements history with an increasing amplitude at each step, consistently with the experimental displacement loading history. It is worth underlining that the length of the upper part of the columns above the spliced sections is different for each case (*i.e.*, 1100 mm, 1500 mm and 1875 mm for the SC-CB1, SC-CB2 and the SC-CB3, respectively). Therefore, considering a target rotation (θ_t) equal to 0.04 rads, the target displacements are equal to 44 mm, 64 mm and 75 mm for the SC-CB1, SC-CB2 and the SC-CB3, respectively.

Global and local responses are monitored to assess how the selected parameters affect the behaviour of each SC-CBs. Hence, the response of each SC-CB is compared among all the configuraions to identify the best design solution in terms of improved self-centring capacity of the joint and minimal yielding of the components. The global response of the joints is evaluated in terms of hysteretic moment-rotation behaviour. Conversely, the local response is analysed by monitoring the following parameter on the column and its components: *i)* the equivalent plastic strain distributions (PEEQ); *ii)* the maximum local plastic strain (ε_{max}) normalized with respect to the ultimate strain (ε_u) of the material; *iii)* the ALLPD (Plastic Dissipated Energy) (*i.e.*, the amount of plastic energy dissipated by the whole connection during the analysis). Additionally, the distributions of the shear forces are illustrated to provide insights into the magnitude of the shear transferred by each component of the SC-CB. It is worth highlighting that, in the PEEQ legend the limit is assumed equal to the yielding strain (ε_y) of the material and the values of the yielding strain (ε_y) and the ultimate strain (ε_u) of the material are assumed respectively equal to 1.2% and 1.67%.

For the sake of brevity, only the global and local result of the SC-CB1 and the SC-CB2 are illustrated, considering the maximum compressive axial load (N_{Max}). The results for the other SC-CBs configurations and the other axial load condition (N_{Min}) are not shown. However, it is worth mentioning that they exhibit a consistent trend with the results shown herein, and the following considerations can be extended to all the cases.

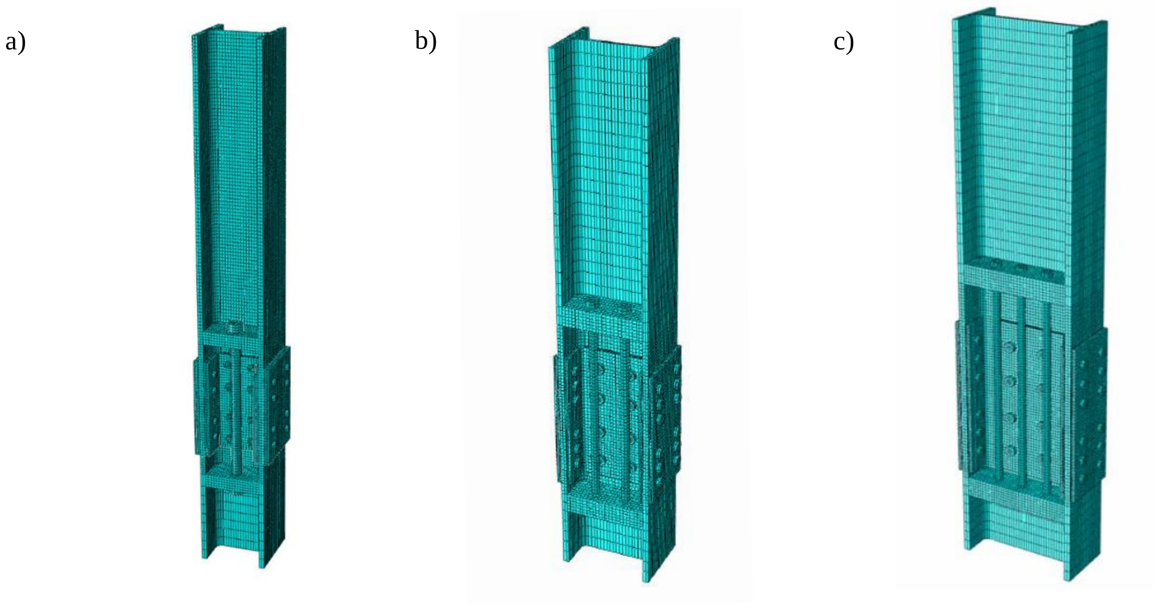

Figure 10: FE models developed in ABAQUS [56]: (a) SC-CB1; (b) SC-CB2; (c) SC-CB3.

4.3 Influence of the thickness of the flanges' plates

Figure 11 compares the moment-rotation hysteretic curves of two SC-CBs (*i.e.*, SC-CB1 in Figure 11(a) and SC-CB2 in Figure 11(b)) in configuration 1 and 2 (*i.e.*, t_{fp} (continuous blue lines) and $2t_{fp}$ (dotted red lines)). These two configurations are equipped by flanges' plates having a thickness of 8 - 16 mm for the SC-CB1 and 12 - 24 mm for the SC-CB2. In addition, the theoretical models (*i.e.*, analytical equations) are also shown with a continuous black line. The global response is shown only for the maximum compressive axial load (N_{Max}). The results in terms of global hysteretic curves for the other axial load condition (N_{Min}) are not shown, as they exhibit a consistent trend with the results shown herein.

The results show that the global response of the connections is not significantly affected by the thickness of the flanges' plates, as expected. In fact, a quite similar hysteretic behaviour is observed between the two configurations for both the SC-CB1 and the SC-CB2. Nevertheless, it is noteworthy that the hysteretic curves of the configurations equipped with the thicker plates show a slightly increasing hardening, confirming the larger bending contribution with respect to the configurations equipped with the thinner plates. However, these results suggest that it is possible to neglect the bending contribution of the flanges' plates in the design phase.

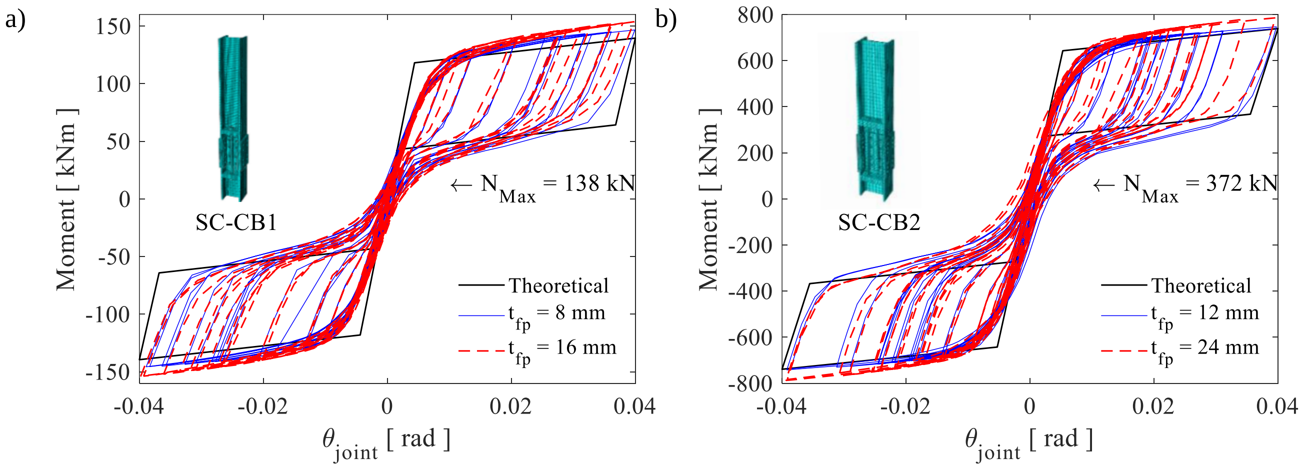

Figure 11: Influence of different thickness of the flanges' plates. Moment-rotation behaviour: (a) SC-CB1; (b) SC-CB2

The local results are illustrated in terms of PEEQ (*i.e.*, equivalent plastic strain) distributions in Figure 12 (a) and (b) only for the SC-CB1 in Configuration 1 and 2 (*i.e.*, t_{fp} equal to 8 mm and 16 mm) respectively. The results show the front and side views (*i.e.*, web and flanges, respectively) of the column at the end of the cyclic analysis (*i.e.*, zero rotation), considering the maximum compressive axial load (N_{Max}). For the sake of brevity, the PEEQ distributions for the other SC-CBs (*i.e.*, SC-CB2 and SC-CB3) and the other axial load condition (N_{Min}) are not shown, as they show a consistent trend with the results shown herein.

Some general considerations can be made regarding the location of the plastic strains for both the configurations. It is observed that some concentrations of slight plastic deformations are located nearby the spliced section, close to the oversized web holes and the flange slots. In addition, slight plastic deformations can be observed in the cover plates and friction shims of the flange FDs, as well as in the bolts' shanks of the flange FDs, not shown due to space constraint. Conversely, the PT bars do not exhibit any plastic strain. It is worth mentioning that these results are consistent with what enforced from the design methodology shown in Section 2.

The comparison of the PEEQ distribution between Figure 12 (a) and (b) provides an understanding of the influence of the thickness of the flanges' plates on the local behaviour of the SC-CB. In particular, the results show that the use of thicker plates leads to an increment of the plastic damage on the column, which is mainly due to their larger stiffness. Therefore, this result suggests that the use of thinner flange plates is beneficial in reducing the strain concentrations on the column.

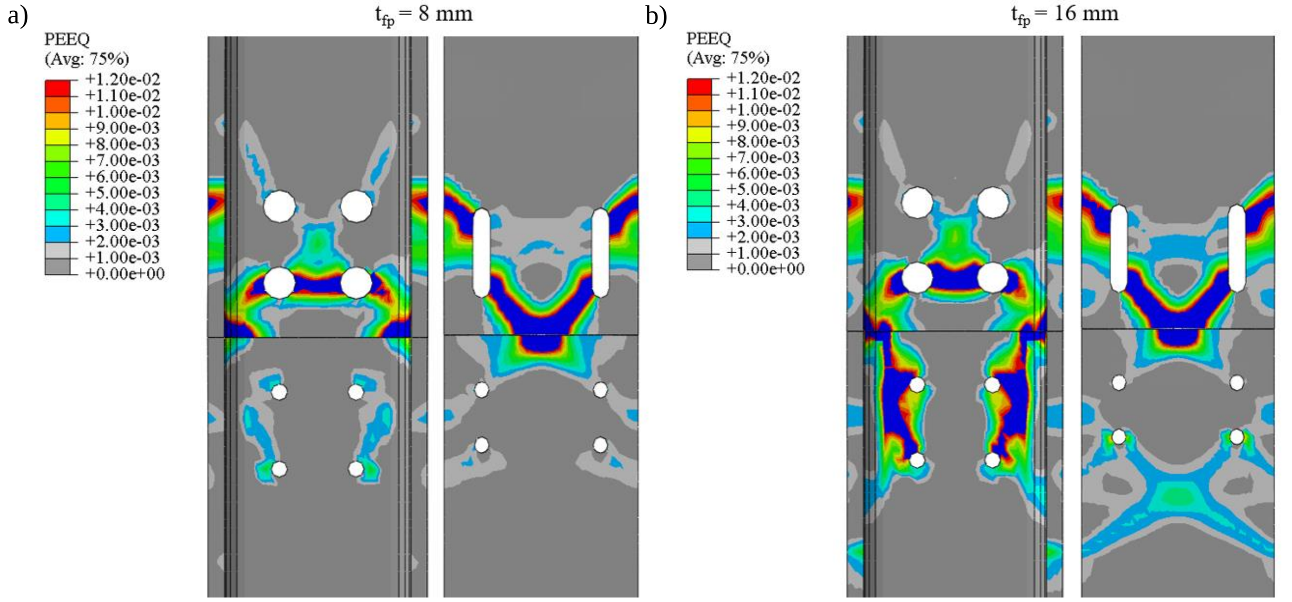

Figure 12: Influence of the thickness of the flanges' plates. PEEQ Distribution at the end of the cyclic analysis for the SC-CB1: (a) Configuration 1; (b) Configuration 2.

The influence of this parameter is confirmed by observing the amount of ALLPD (Dissipated Plastic Energy) shown in Figure 13 (a) and by the normalized maximum local strain (ε_{max}) shown in Figure 13 (b) for the SC-CB1 in Configuration 1 and 2 (*i.e.*, t_{fp} equal to 8 mm and 16 mm). Results are shown for the maximum design axial load (N_{Max}) and for the minimum design axial load (N_{Min}) in thicker and thinner lines, respectively.

The comparison between the responses of the SC-CB1 in the two configurations shows that the use of thinner flange plates allows a reduction of the amount of the dissipated plastic energy, and this is more evident when the SC-CB is subjected to the maximum design axial load. Moreover, it is worth stressing that, even though a greater energy dissipation is generally a benefit, this parameter corresponds to the whole energy dissipated by all the components which are expected to remain in the elastic range. Thus, a minor dissipation of the plastic energy represents an advantage for the SC-CB connection. Additionally, the comparison of the normalized maximum local strains (ε_{max}) between the two configurations highlights that the increase of the thickness of the flanges' plates leads to an increase of the normalized maximum local strain (*e.g.*, from 0.15 to 0. 23 for the SC-CB1 subjected to N_{Max}) and consequently to an increasing damage on the column, confirming what previously observed by the PEEQ distribution in Figure 12.

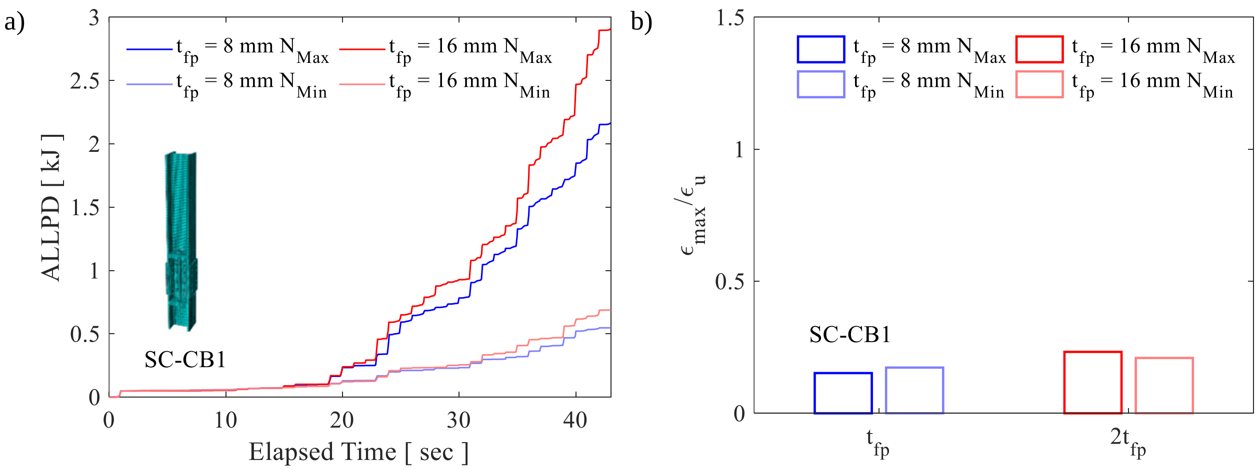

Figure 13: Influence of the thickness of the flanges' plates. (a) Plastic Dissipated Energy (ALLPD); (b) Maximum local strains.

4.4 Influence of the design shear load

Figure 14 illustrates the moment-rotation hysteretic behaviour two SC-CBs (*i.e.*, SC-CB1 in Figure 14 (a) and SC-CB2 in Figure 14 (b)) in configurations 1 (*i.e.*, design shear load percentage carried by the web FDs equal to 100%) and in configurations 3, 4 and 5. These latter are obtained by considering the design shear load percentage carried by the web FDs equal to 75%, 50% and 0%, as previously reported in Table 8. In addition, the theoretical models (*i.e.*, analytical equations) are also shown with a continuous black line. The global response is shown only for the maximum compressive axial load (N_{Max}). The results in terms of global hysteretic curves for the other axial load condition (N_{Min}) are not shown, as they exhibit a consistent trend with the results shown herein. Results show that a similar hysteretic behaviour is observed for all the considered configurations for both the SC-CB1 and the SC-CB2. These considerations demonstrate that, as for what observed in Figure 11, the considered parameter does not alter the global hysteretic behaviour of the SC-CBs.

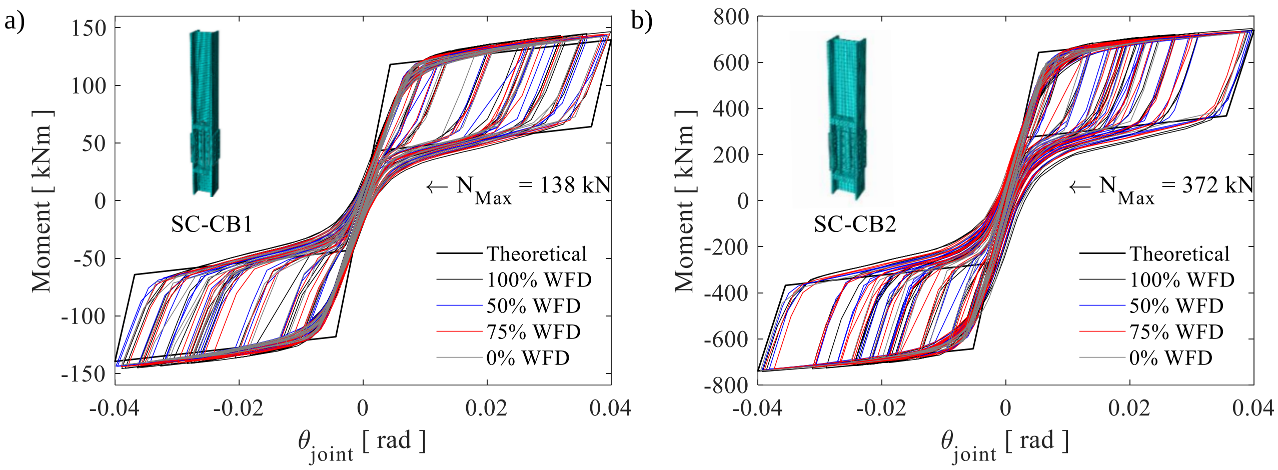

Figure 14: Influence of the design shear load. Moment-rotation behaviour: (a) SC-CB1; (b) SC-CB2

The local results corresponding to Figure 14 (a) are illustrated in Figure 15 only for SC-CB1 in terms of PEEQ (*i.e.*, equivalent plastic strain) distribution on the column's web. The results are evaluated at the end of the cyclic FE analysis (*i.e.*, zero rotation) considering the maximum compressive axial load (N_{Max}). By the comparison of the PEEQ distributions on the column's web in the different configurations, it is possible to observe a clear dependence between the considered design parameter with the strain distributions. In particular, it is evidenced that the extension of the damage is higher in configuration 1 (*i.e.*, 100% WFD) and it tends to proportionally reduce with the others. These results suggest that designing the web FD to carry a minor percentage (*i.e.*, 75%, 50% or 0%) of the design shear load represents an efficient design solution which reduces the strain concentrations on the column.

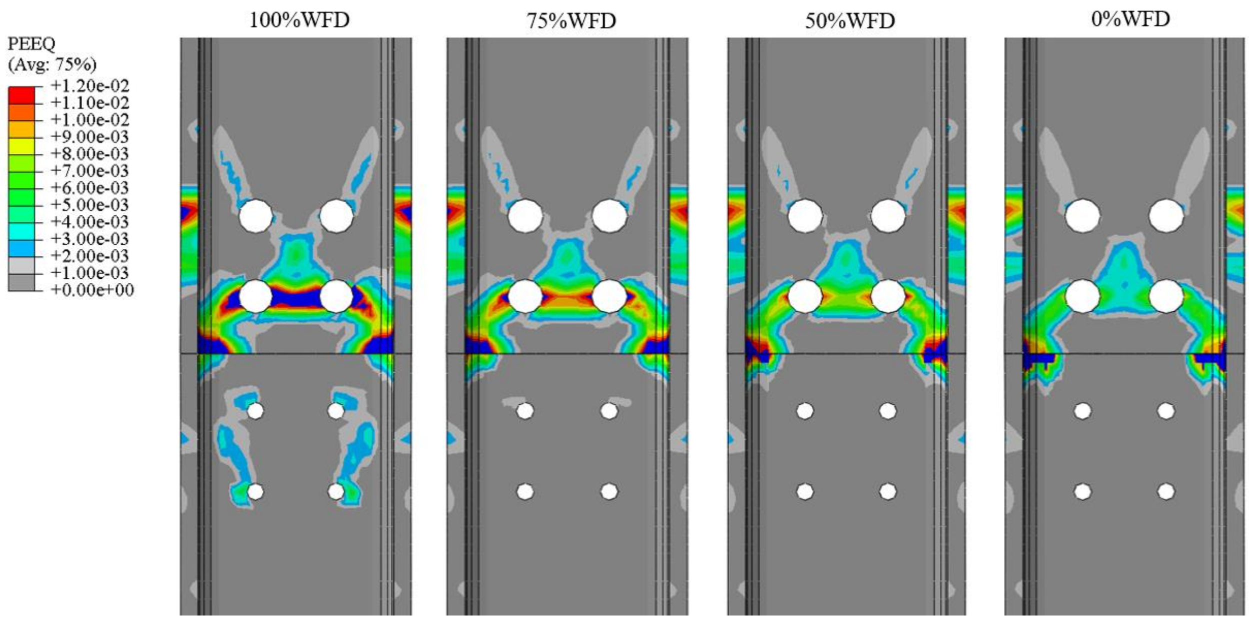

Figure 15: Influence of the design shear load. PEEQ Distribution at the end of the cyclic analysis for the SC-CB1

The sensitivity of the local response to this parameter observed in Figure 15 is confirmed by observing the amount of ALLPD (Dissipated Plastic Energy) shown in Figure 16 (a) for the SC-CB1 in configurations 1, 3, 4 and 5 (*i.e.*, design shear load percentage carried by the web FDs equal to 100%, 75%, 50 % and 0%). Results highlight that there is a significant reduction of the amount of the dissipated plastic energy obtained by designing the web FD to carry a minor percentage of the design shear load. It is worth underling that this effect is more relevant when the SC-CB is subjected to the maximum design axial load. Conversely, slight differences can be observed by comparing the results in the same configurations when subjected to the minimum design axial load.

Additionally, Figure 16 (b) shows the maximum local strain (ε_{max}) normalized with respect to the ultimate strain of the material (ε_u) for the SC-CB1. It is observed a clear trend of the design shear percentage carried by the web FDs on the local plastic damage of the connection. In particular, the maximum local strain assumes the lowest value in configuration 4 (*i.e.*, 50% WFD). Conversely, the highest value of the maximum local strain occurs in Configuration 5 (*i.e.*, 0% WFD). This trend is consistent for both the design axial load conditions. Consequently, the results shown in Figure 16 suggest that the design choice of entrusting to the web FDs the 50% of the design shear load represents the optimal design configuration in terms of local damage reduction on the column and minimal dissipated plastic energy.

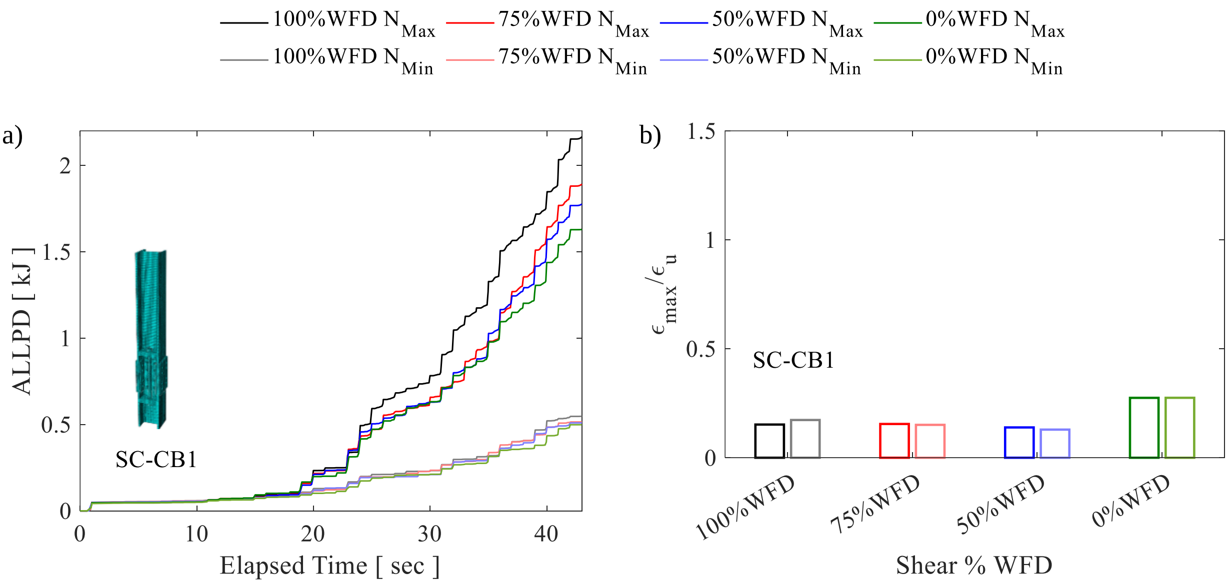

Figure 16: Influence of the design shear load. (a) Plastic Dissipated Energy (ALLPD); (b) Maximum local strains.

Further considerations can be made to provide information about the transfer mechanism of the shear force among the components, while offering insights into the magnitude of the shear transferred by each component, which cannot be predicted in the design procedure. Figure 17 (a) and (b) show the distributions of the shear forces among the components for the SC-CB1 in Configuration 1 (*i.e.*, 100% WFD) and in Configuration 4 (*i.e.*, 50%WFD) respectively. Results are shown only for one single SC-CB, however the following considerations can be extended to all cases. The SC-CB1 in Configuration 1 (Figure 17 (a)) is characterized by levels of maximum shear forces transferred by the web FDs of about the 50% of the total shear, while the flange FDs reach values close to the 80% of the total shear. This result highlight that there is a significant contribution of the flange FDs, mainly due to the larger stiffness provided by the flanges' plates, which transfer larger shear forces, compared to those transferred by the web plates. This effect is also due to the socket/contact forces. Conversely, the distribution of the shear forces of the SC-CB1 in Configuration 4 (Figure 17 (a)) exhibits a different behaviour. In particular, the web FDs carry less than the 50% of the design shear force, while there is a higher shear contribution of the flange FDs with respect to configuration 1 and, consequently, it is observed a smoother transfer of the shear forces on the column. By the comparison of the two distributions, it is evidenced that designing the web FD to carry 50% of the design shear load represents a benefit in terms of shear distribution, confirming the previous observations.

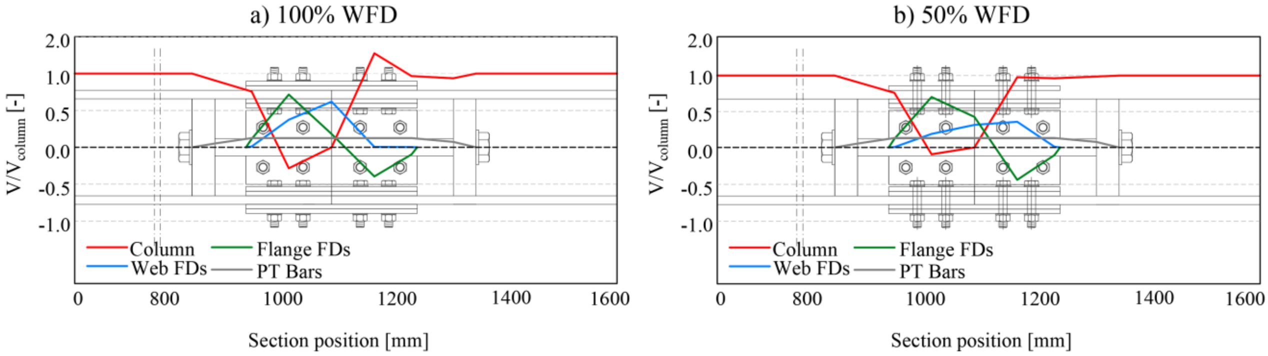

Figure 17: Distribution of shear of the SC-CB1 at 0.04 rad rotation: (a) 100%WFD; (b) 50%WFD.

4.5 Influence of the design axial load

In this work, the design axial force of the SC-CB is assumed to be constant considering two limit conditions (*i.e.*, the max ($N_{Ed,max}$).and min compressive axial force ($N_{Ed,min}$). However, in the design procedure it has been highlighted how the moment-rotation behaviour of the SC-CB is strongly affected by the axial force and therefore, two main issues have been discussed and analysed in Section 2. Firstly, the assumption of the adoption of a constant axial force is clearly not reproducing the real load situation of all the columns of a MRF, due to large axial force fluctuations that happen during the seismic event. Successively, it has been evidenced that the adoption of the min compressive axial force ($N_{Ed,min}$) as the design axial load for the SC-CB may represent an overconservative design approach, thus leading to an overestimation/oversizing of the components belonging to the self-centring system (*i.e.*, the necessary number and the necessary pre-load force of the PT bars). In other words, this may represent a disadvantage in terms of increasing cost of material, cost of construction and technological issues, especially for mid or high-rise MRFs, where the external columns are subjected to large axial force variations. One of the objectives of this work is to clarify this aspect, by considering the axial load due to the gravity loads (N_g) as the design axial load and to evaluate the self-centring capacity when the SC-CB connection is subjected to a variable axial load input.

Therefore, the validity of the aforementioned design choice is investigated by developing an additional design configuration of the SC-CB, obtained by assuming the axial load due to the gravity loads (N_g) as the design axial force and following the design methodology shown in Section 2. Hence, an additional FE model of the SC-CB is developed in ABAQUS [56] by following the validated methodology defined in Section 3. The global response of the SC-CB is analysed when the connection is subjected to a real axial load history of the column extracted from the reference MRF, to assess the influence of the axial load variability on the response of the SC-CB connection, as well as on the self-centring behaviour of each SC-CB. Table 9 shows an overview of the maximum, minimum and gravity design axial forces for each SC-CB. In addition, the axial loads ratios referred to the external columns (*i.e.*, $N_{g,ext}/N_{Pl}$) are also reported.

Table 9: Input design axial load input for the additional configurations

Specimen	$N_{Ed,Max}$ [kN]	$N_{Ed,Min}$ [kN]	$N_{g,ext}$ [kN]	$N_{g,int}$ [kN]	$N_{g,ext}/N_{Pl}$ [-]
SC-CB1	+138	-127	+15	+15	0.0054
SC-CB2	+372	-183	+95	+198	0.0135
SC-CB3	+400	-807	+201	+405	0.0209

Note: negative values are for tension; positive values are for compression.

Numerical FE models of the three case-study MRFs upgraded with the SC-CB connections designed in Section 2 are implemented in OPENSEES [60] and Non-Linear Time History Analyses (NLTHAs) are successively performed by considering several ground motions records. The FE modelling strategy and the ground motion selection procedure are developed consistently with the methodology proposed in Elettore *et al.* 2021 [50]. The global response of the three MRFs equipped with the SC-CBs is studied to investigate the variability of the axial load in the first storey columns of the selected MRFs. Successively, the real axial load time history of the external column is assumed as an input parameter for the FE analysis in ABAQUS [56]. The input parameters are: *i)* the axial load time history of the external column; *ii)* the displacement time history of the external column evaluated at the spliced section. This latter is evaluated as the sum of the displacements obtained by the joint rotation and by the elastic contribution of the column.

In this work, the SC-CB1 and the corresponding MRF1 are considered as the reference case-study, as the axial load ratio is the lowest amongst all the reference MRFs, as highlighted in Table 9. It is worth reminding that the other results obtained by the NLTHAs are not shown as the attention of this work is focused only on the axial load history. Results of the NLTHAs are shown for a single ground motion record at the ULS intensity, for the sake of brevity. However, it is due to mention that the other results show a consistent trend with the results illustrated hereafter.

Figure 18 (a) shows the axial load time history of one of the first story external columns of the MRF1. The values corresponding to the gravity axial force (N_g) as well as the maximum ($N_{Ed.max}$) and minimum ($N_{Ed.min}$) design axial force of the SC-CB1 are reported with dotted lines. Additionally, the joint rotation (θ_{joint}) time history of the SC-CB1 is illustrated in Figure 18 (b). It is worth noting that the joint rotation experiences values which are lower than the target rotation of the joint, assumed equal to 0.04rads.

Figure 19 shows the hysteretic curve of the SC-CB1 (i.e., continuous red line) designed with the axial load due to gravity loads (N_g) and subjected to the variable axial load input illustrated in Figure 18 (a). In addition, the backbone curves of the moment-rotation behaviour of the SC-CB1 obtained considering the constant maximum ($N_{Ed.max}$), the minimum ($N_{Ed.min}$) compressive axial force and the gravity axial force (N_g) are depicted in black, grey and blue dotted lines, respectively. Results show that the hysteretic curve of the SC-CB1 follows the envelopes corresponding to the gravity and the minimum design axial loads. In addition, it is observed a full self-centring behaviour with a very low residual rotation, therefore the self-centring condition is still satisfied. Hence, this result suggests that it is possible to assume the gravity load as the design axial load of the SC-CB, as the self-centring condition is satisfied.

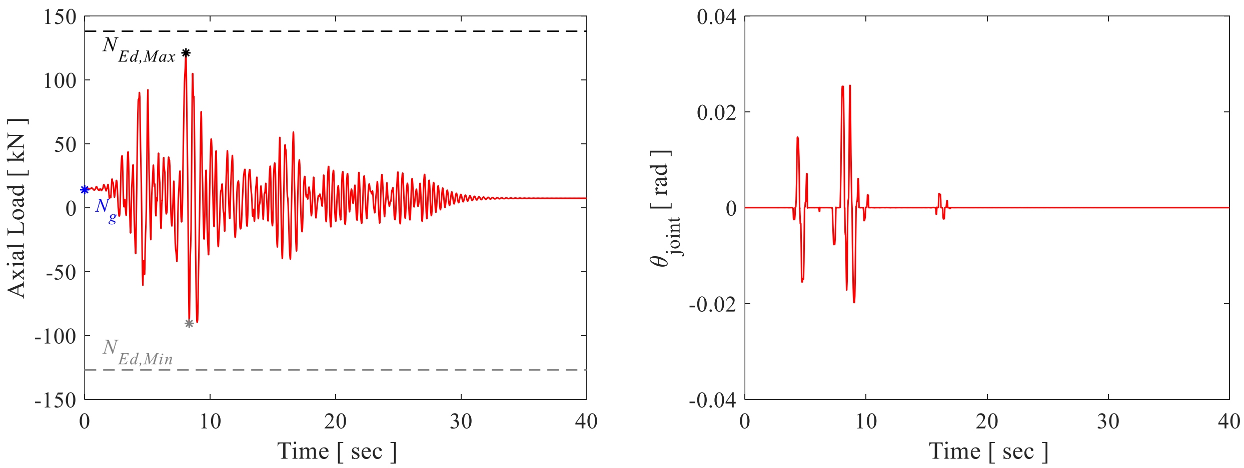

Figure 18: Results of one column of the MRF-1: (a) Axial load time history; (b) SC-CB Rotation time history

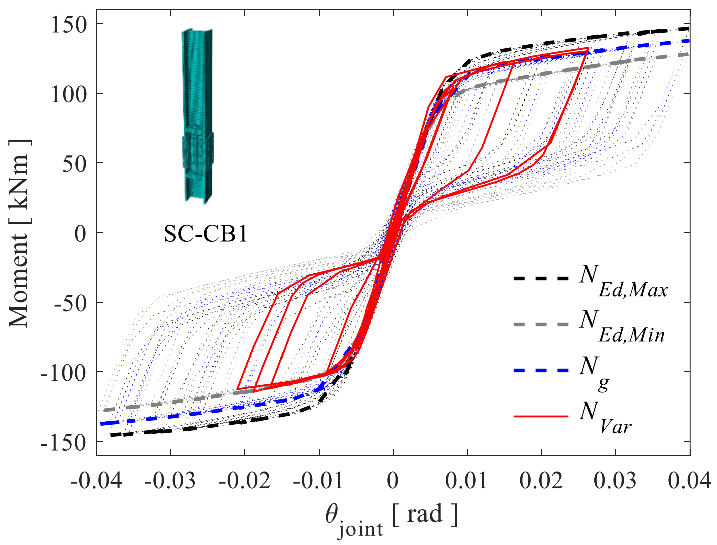

Figure 19: Influence of the axial load variability. Moment rotation behaviour of the SC-CB1

5 CONCLUSION

The present study investigates a previously proposed Self-Centring Column Base (SC-CB) by means of a parametric Finite Element (FE) analysis with the purpose of providing insight to the global and local behaviour under cyclic loading, while proposing improvements to the existing design procedure. An experimental campaign of a previously tested SC-CB is summarised first, and an advanced FE model is developed in ABAQUS and validated against the experimental results. The results of the FE validation show that the model correctly predicts the global hysteretic response observed during the experimental tests, providing useful insights into the characterization of the local behaviour of the SC-CB connection. A parametric FE analysis is successively conducted in ABAQUS selecting three SC-CBs belonging to different case-study Moment Resisting Frames (MRFs), to investigate the scale effect on different geometrical configurations. A matrix of sixteen different configurations is considered for each SC-CB, obtained by varying three design properties of the joints (*i.e.*, the thickness of the flanges' plates, the design shear load, and the design axial load). For each configuration, global and local parameters are monitored to investigate the influence of these parameters on the global and local behaviour of the SC-CB connections. The results are compared for all the configurations, to identify the best design solution in terms of improved self-centring capacity of the joint and minimal yielding of the components Results from the FE parametric analysis provide a more comprehensive scenery on the assumptions and limitations of the design methodology, highlighting the crucial aspects of the design procedure and suggesting additional recommendations to improve the design requirements.

Based on the obtained outcomes, the following remarks can be drawn: *i)* The global hysteretic response of the connections is not affected by the considered design parameters while the local behaviour is significantly influenced; *ii)* The use of thinner flange plates represents a benefit in terms of reduction of the local plastic damage on the column while also allowing a reduction of the amount of the dissipated plastic energy; *iii)* There is a clear tendency of the design shear percentage entrusted by the web FDs on the amount of the dissipated plastic energy of the whole connection; *iv)* Designing the web FD to carry a minor percentage (*i.e.*, 75%, 50% or 0%) of the design shear load represents an efficient design solution which reduces the strain concentrations on the column; *v)* The optimal design configuration in terms of damage reduction is represented by the connection equipped with the thinner flanges' plates and designing the web FD to carry the 50% percentage of the design shear load; *vi)* The self-centring condition is still satisfied considering the gravity axial force as design axial load for the SC-CB.

6 REFERENCES

1 F.M. Mazzolani, V. Piluso, Theory and Design of Seismic Resistant Steel Frames. London, UK, 1996.

2 C. Faella, V. Piluso, G. Rizzano, Structural steel semirigid connections. CRC Press, Boca Raton (FL), 2000.

3 EN 1998-1, Eurocode 8: Design of structures for earthquake resistance – Part 1: General rules, seismic actions and rules for buildings, *European Committee for Standardization*, Brussels.

4 ANSI/AISC 341-16 Seismic provisions for structural steel buildings. *American Institute of Steel Construction*, Chicago, USA, 2016.

5 ASCE/SEI 7–16, Minimum Design Loads and Associated Criteria for Buildings and Other Structures, American Society of Civil Engineers, 2017.

6 J. McCormick, H. Aburano, M. Nakashima, Permissible residual deformation levels for building structures considering both safety and human elements, 14th World Conf. Earthq. Eng. 12-17 Oct 2008, Beijing, China.

7 F. Freddi, V. Novelli, R. Gentile, E. Veliu, A. Andonov, S. Andreev, F. Greco, E. Zhuleku, Observations from the 26th November 2019 Albania Earthquake: the Earthquake Engineering Field Investigation Team (EEFIT) mission. Bull. Earth. Eng., 19 (2021) 2013-2044.

8 S. Pampanin, Reality-Check and renewed challenges in Earthquake Engineering: implementing low-damage systems from theory to practice. Bull New Zealand Society Earthq Eng. 45(4) (2012) 137-160.

9 N.B. Chancellor, M.R. Eatherton, D.A. Roke, T. Akbas, Self-Centering Seismic Lateral Force Resisting Systems: High Performance Structures for the City of Tomorrow, Buildings 4 (2014) 520–548.

10 F. Freddi, C. Galasso, G. Cremen, A. Dall'Asta, L. Di Sarno, A. Giaralis, L.F. Gutiérrez-Urzúa, C. Málaga-Chuquitaype, S. Mitoulis, C. Petrone, A. Sextos, L. Sousa, K. Tarbali, E. Tubaldi, J. Wardman, G. Woo, Innovations in Earthquake Risk Reduction for Resilience: Recent Advances and Challenges, International Journal of Disaster Risk Reduction, 60 (2021) 102267.

11 C. Fang, W. Wang, C. Qiu, S. Hu, G.A. MacRae, M.R. Eatherton, Seismic resilient steel structures: A review of research, practice, challenges and opportunities. J. Constr. Steel Res. 191 (2022) 107172.

12 X. Huang, X. Zhou, Y. Wang, R. Zhu, Development of resilient friction beams and application to moment-resisting frames. J. Build. Eng. 45 (2022) 103494

13 Y. Shen, F. Freddi, J. Li, Experimental and numerical investigates on seismic behavior of socket connections and hybrid connections for PCFT bridge columns. Eng. Stru. 253 (2022) 113833.

14 J. Ricles, R. Sause, M. Garlock, C. Zhao, Posttensioned Seismic-Resistant Connections for Steel Frames, J. Struct. Eng. 127(2) (2001) 113–121.

15 C. Christopoulos, A. Filiatrault, C-M. Uang, B. Folz, Posttensioned energy dissipating connections for moment-resisting steel frames, J. Struct. Eng. 128(9) (2002) 1111–20.

16 H.H. Khoo, C. Clifton, J. Butterworth, G. MacRae, S. Gledhill, G. Sidwell, Development of the self-centering sliding hinge joint with friction ring springs, J. Constr. Steel Res. 78 (2012) 201–211.

17 G. Vasdravellis, T.L. Karavasilis, B. Uy, Large-scale experimental validation of steel posttensioned connections with web hourglass pins. J. Struct. Eng. 139 (2012) 1033–1042.

18 L. Pieroni, F. Freddi, M. Latour, Effective placement of Self-Centering Damage-Free Connections for Seismic-Resilient Steel Moment Resisting Frames, Earth. Eng. Stru. Dyn. (2022)

19 M. Latour, G. Rizzano, Full strength design of column base connections accounting for random material variability, Eng. Struct. 48 (2013) 458–71.

20 P.T. Rodas, F. Zareian, A. Kanvinde, Hysteretic model for exposed column-base connections, J. Struct. Eng.; 142 (12) (2016) 1–14.

21 A. Elkady, G. Guell, D.G. Lignos, Proposed methodology for building-specific earthquake loss assessment including column residual axial shortening, Earthq. Eng. Struct. Dyn. 49 (2020) 339–355.

22 H. Inamasu, A. de Castro e Sousa, G. Guell, D.G. Lignos: Anchor-yield exposed column bases for minimizing residual deformations in seismic-resistant steel moment frames, Earth. Eng. Struc. Dyn. 50 (2021)1083–1100.

23 R. Tremblay, P. Timler, M. Bruneau, A. Filiatrault, Performance of steel structures during the 1994 Northridge earthquake. J. Civil. Eng. 22(2) (1995) 338–60.

24 M. Nakashima, K. Inoue, M. Tada, Classification of damage to steel buildings observed in the 1995 Hyogoken-Nanbu earthquake. Eng. Struct. 20(4–6) (1998) 271–81.

25 M. Midorikawa, I. Nishiyama, M. Tada, T. Terada, Earthquake and tsunami damage on steel buildings caused by the 2011 Tohoku Japan earthquake. Proceedings of the International Symposium on Engineering Lessons Learned From the 2011 Great East Japan Earthquake. Japan Association for Earthquake Engineering, Tokyo, Japan, 2012.

26 M. Latour, G. Rizzano, A theoretical model for predicting the rotational capacity of steel base joints, Eng. Struct. 91 (2013) 89–99.

27 F. Zareian, A. Kanvinde, Effect of column-base flexibility on the seismic response and safety of steel moment-resisting frames, Earth. Spectra 29 (2013) 1537–1559

28 J.R. Garcia, A. Kanvinde, Effect of column base flexibility on residual drift demands of low-rise steel moment-resisting frames. The 2013 World Congress on Advances in Structural Engineering and Mechanics (ASEM13). Jeju, Korea, September 8-12, 2013

29 P.A. Torres-Rodas, F. Flores, F. Zareian, Seismic response of steel moment frame considering gravity system and

column base flexibility, Proc. 11th US Natl. Conf. Earthq. Eng., June 25–29, Los Angeles, USA, 2018.
30 G.A. MacRae, C.R. Urmson, W.R. Walpole, P. Moss, K. Hyde, G.C. Clifton, Axial Shortening of Steel Columns in Buildings Subjected to Earthquakes, Bulletin of The New Zealand Society for Earthq. Eng. 42(4) (2009) 275–287.
31 J. Borzouie, G.A. MacRae, J.G. Chase, G.W. Rodgers, G.C. Clifton. Experimental studies on cyclic performance of CB strong axis – aligned asymmetric friction connections. J. Struct. Eng. (ASCE), 142(1) (2016) 1–10.
32 T. Takamatsu, H. Tamai Non-slip-type restoring force characteristics of an exposed-type CB. J. Constr. Steel Res. 61(7) (2005) 942–961.
33 M. Ikenaga, T. Nagae, M. Nakashima, K. Suita, Development of CBs having self-centering and damping capability. 5th Int. Conf. on Behaviour of Steel Struct. in Seismic Areas 2006, Yokohama, Japan.
34 H. Mackinven, G.A. MacRae, S. Pampanin, G.C. Clifton, J. Butterworth, Generation four steel moment frame joints. 8th Pacific Conf. on Earthq. Eng. 2007, Singapore.
35 C. Chou, J.H. Chen, Analytical model validation and influence of CBs for seismic responses of steel post-tensioned self-centering MRF systems. Eng. Struct. 33(9) (2011) 2628–2643.
36 H. Chi, J. Liu, Seismic behaviour of post-tensioned CB for steel self-centering moment resisting frame, J. Constr. Steel Res. 78 (2012) 117–130.
37 T. Yamanishi, K. Kasai, T. Takamatsu, H. Tamai, Innovative column-base details capable of tuning rigidity and strength for low to medium-rise steel structures. 15th World Conf. on Earthq. Eng. 2012, Lisbon, Portugal.
38 F. Freddi, C.A. Dimopoulos, T.L. Karavasilis, Rocking damage-free steel CB with Friction Devices: design procedure and numerical evaluation, Earthq. Eng. Struct. Dyn. 46 (2017) 2281–2300.
39 F. Freddi, C.A. Dimopoulos, T.L. Karavasilis, Experimental evaluation of a rocking damage-free steel CB with friction devices, J. Struct. Eng. 146(10) (2020) 04020217
40 V. Kamperidis, T.L. Karavasilis, G. Vasdravellis, Self-centering steel CB with metallic energy dissipation devices, J. Constr. Steel Res. 149 (2018) 14–30.
41 X.T. Wang, C.D. Xie, L.H. Lin, J. Li, Seismic behaviour of self-centering concrete-filled square steel tubular (CFST) CB. J. Constr. Steel Res. 156 (2019) 75–85.
42 M. Latour, G. Rizzano, A. Santiago, L. Da Silva, Experimental response of a low-yielding, self-centering, rocking CB joint with friction dampers, Soil Dyn. Earthq. Eng. 116 (2019) 580–592.
43 B. Wang, S. Zhu, C-X Qui, H. Jin, High-performance self-centering steel columns with shape memory alloy bolts: Design procedure and experimental evaluation. Eng. Struc. 182 (2019) 446-458
44 B. Wang, H. Jiang, J. Wang, Numerical simulation and behavior insights of steel columns with SMA bolts towards earthquake resilience. J. Constr. Steel Res. 161 (201) 285-295
45 M. Latour, M. D'Aniello, M. Zimbru, G. Rizzano, V. Piluso, R. Landolfo, Removable friction dampers for low-damage steel beam-to-column joints, Soil Dyn. Earthq. Eng. 115 (2018) 66–81.
46 G.F. Cavallaro, A. Francavilla, M. Latour, V. Piluso, G. Rizzano, Experimental behaviour of innovative thermal spray coating materials for FREEDAM joint. Composites Part B 115 (2017) 289-299
47 G.F. Cavallaro, A. Francavilla, M. Latour, V. Piluso, G. Rizzano, Cyclic behaviour of friction materials for low yielding connections. Soil Dyn. Earthq. Eng. 114 (2018) 404–423.
48 A.F. Santos, A. Santiago, M. Latour, G. Rizzano, L.S. da Silva, Response of friction joints under different velocity rates. J. Const. Steel Res. 168 (2020) https://doi.org/10.1016/j.jcsr.2020.106004
49 M. D'Antimo, M. Latour, J.F. Demonceau, Drop-weight impact tests on free from damage beam to column connections, J. Constr. Steel Res. 192 (2022) https://doi.org/10.1016/j.jcsr.2022.107215
50 E. Elettore, F. Freddi, M. Latour, G. Rizzano, Design and analysis of a seismic resilient steel moment-resisting frame equipped with damage-free self-centring column bases. J Constr Steel Res. 179 (2021)106543.
51 E. Elettore, A. Lettieri, F. Freddi, M. Latour, G. Rizzano, Performance-based assessment of seismic-resilient steel moment resisting frames equipped with innovative column base connections. Structures 32 (2021)1646-1664.
52 R. Tartaglia, M. D'Aniello, G.A. Rassati, J.A. Swanson, R. Landolfo, Full strength extended stiffened end-plate joints: AISC vs recent European design criteria, Eng. Struct. 159 (2018) 155–71
53 R. Tartaglia, M. D'Aniello, G.A. Rassati, Proposal of AISC-compliant seismic design criteria for ductile partially restrained endplate bolted joints. J. Constr. Steel Res. 159 (2019) 364-383
54 M. D'Aniello, R. Tartaglia, S. Costanzo, R. Landolfo, Seismic design of extended stiffened end-plate joints in the framework of Eurocodes, J. Constr. Steel Res. 128 (2017) 512–527.
55 A.B. Francavilla, M. Latour, V. Piluso, G. Rizzano, Design criteria for beam-to-column connections equipped with friction devices. J. Constr. Steel Res. 172 (2020)106240.
56 ABAQUS/Standard and ABAQUS/Explicit – Version 2017. ABAQUS Theory Manual, Dassault Systems, 2016.
57 EN 1993-1-8, Eurocode 3: Design of steel structures, Part 1-8: Design of steel structure: General rules and rules for buildings, 2005, European Committee for Standardization, Brussels.
58 EN 1993-1-1, Eurocode 3: Design of steel structures, Part 1-1: Design of steel structures: Design of joints, 2005, European Committee for Standardization, Brussels.
59 EN 1090-2. Execution of steel structure and aluminium structure: technical requirements for steel structures.
60 S. Mazzoni, F. McKenna, M.H. Scott, G.L. Fenves OpenSEES: Open System for earthquake engineering simulation, Pacific Earthquake Engineering Research Centre (PEER), 2009, Univ. of California, Berkley, CA